Hybrid iron montmorillonite nano-particles as an oxygen scavenger

Erland-Modeste Kombaya-Touckia-Linin, Sebastien Gaucel, Moulay Tahar Sougrati, Khadijeh Khederlou, Nakry Pen, Lorenzo Stievano, Nathalie Gontard, Valérie V. Guillard

Hybrid Iron Montmorillonite Nano-Particles as an oxygen scavenger

Erland-Modeste Kombaya-Touckia-Linin, Sébastien Gaucel, Moulay T. Sougrati, Khadijeh Khederlou, Nakry Pen, Lorenzo Stievano, Nathalie Gontard, Valérie Guillard

PII: S1385-8947(18)31884-9
DOI: https://doi.org/10.1016/j.cej.2018.09.164
Reference: CEJ 20003

To appear in: *Chemical Engineering Journal*

Received Date: 3 July 2018
Revised Date: 23 August 2018
Accepted Date: 21 September 2018

Please cite this article as: E-M. Kombaya-Touckia-Linin, S. Gaucel, M.T. Sougrati, K. Khederlou, N. Pen, L. Stievano, N. Gontard, V. Guillard, Hybrid Iron Montmorillonite Nano-Particles as an oxygen scavenger, *Chemical Engineering Journal* (2018), doi: https://doi.org/10.1016/j.cej.2018.09.164

Title: Hybrid Iron Montmorillonite Nano-Particles as an oxygen scavenger

Authors: Erland-Modeste Kombaya-Touckia-Linin[1], Sébastien Gaucel[1], Moulay T. Sougrati[2], Khadijeh Khederlou[1], Nakry Pen[1], Lorenzo Stievano[2], Nathalie Gontard[1], Valérie Guillard[1]*,

[1] UMR « Ingénierie des Agropolymères et Technologies Emergentes », INRA, Univ. Montpellier, Montpellier SupAgro, CIRAD, Montpellier, France.

[2] Institut Charles Gerhardt Montpellier, Univ. Montpellier, CNRS, Montpellier, France.

*Corresponding author: valerie.guillard@umontpellier.fr, tel: +33(0)4 99 61 24 32

Abstract (200 mots). Iron nanoparticles supported on montmorillonite (MMT-Fe) were synthesized via the reduction by sodium borohydride of iron salts dissolved in a suspension of MMT. The MMT-Fe black powder collected after the evaporation of the solvent was analysed by Transmission Electron Microscopy, which revealed the formation of aggregates of metallic nanoparticles with an average size of 57 ± 17 nm dispersed on the surface of MMT. According to the X-ray diffraction, no iron ions are intercalated in the interlayer spacing of MMT, and no other crystalline species are formed. ^{57}Fe Mössbauer spectroscopy evidences the formation of mainly zero valent iron in the form of iron boride. The O_2 absorption kinetic of the synthesized powders was found to follow a second-order law. The study of the O_2 absorption properties of as-synthesized, dried and stored (40 days) powders shows reaction constant (k), coefficient of proportionality (n) and O_2 absorption capacities of the same order of magnitude. The O_2 absorption capacity of the as-synthesized, dried and stored powders were found equal to 0.20 ± 0.01, 0.14 ± 0.03 and 0.09 ± 0.00 g O_2 per g of iron, respectively. The initial absorption rate was found within the range [0.5 - 1.5] % O_2 min^{-1} g^{-1}.

Keywords: Iron nanoparticles; Iron boride; Montmorillonite; Oxygen absorption kinetics; modelling ; chemical synthesis, ^{57}Fe Mössbauer spectroscopy

1. Introduction

Modified atmosphere packaging (MAP) is one of the main technological solutions to protect food from oxygen and the related oxidation reactions, which are among the main causes of food deterioration. One of the advantages of MAP is that it avoids adding preservatives (*e.g.*, antioxidants) to the food product [1–3]. A specifically modified atmosphere can be obtained either by flushing the desired gas composition into the packaging headspace, or by using gas absorbers (*e.g.*, O_2 or CO_2 scavengers) or emitters in combination with high barrier films. To achieve the required barrier properties, it is necessary to combine several materials in a multilayer structure which is expensive and often difficult to recycle due to its complex composition, raising serious issues about its end-of-life management [4].

To promote the use of monolayer films, easier to recycle and less expensive than the multilayer ones, a great deal of research has been devoted to improve the barrier properties toward oxygen of monolayer materials derived either conventionally from oil or from innovative biosources. A large part of this research has been devoted to the development and optimization of nanocomposite films. The introduction of impermeable platelets, such as clay nanoparticles that inhibit O_2 diffusion by increasing the tortuosity of the system, into the neat matrix is a promising approach. Several reviews are available on this topic [5–9]. These impermeable platelets, when appropriately exfoliated and dispersed in the matrix with their surface oriented perpendicular to the direction of the gas diffusion path, create a so-called “passive” barrier effect. However, this decrease of permeability is not always sufficient for application to food packaging because it is extremely challenging to achieve both good dispersion and regular arrangement of the nanoplatelets within the polymer matrix [9] An alternative strategy is to combine a “passive” barrier with an “active” one by introducing in the polymer matrix, in addition to nanoclays, a fraction of O_2 scavenger particles. Among different materials with such properties, zerovalent iron nanoparticles (nano-Fe^0) are very

promising owing to their superior reactivity, connected to their high specific surface area and strong reducing power [10,11]. Among all engineered nanoparticles, nano-Fe^0 are certainly one of the most studied materials for environmental [12–17] or medical [18,19] applications. Investigation of their potential use as oxygen scavenger in packaging application is however more recent. For instance, Mu et al. [20] produced oxygen scavenger materials based on iron nanoparticles, and observed an O_2 absorption rate ten times higher with their nanosised system than with conventional iron metal powder. These authors, however, unfortunately did not provide a full characterization of their iron anoparticles, and therefore could not provide a precise relationship between phase speciation and observed absorption kinetics. A few previous studies also dealt with the use of iron as oxygen scavenger additive in polymers, but not with nanosized materials [21,22]. Recently, Foltynowicz et al. [23] produced nanostructured O_2 scavengers by including Fe nanoparticles prepared by liquid phase reduction within a silicon matrix. Such materials displayed a reaction rate two to three times higher than conventional iron powder at 100% relative humidity. The two essential key parameters for a typical O_2 scavenger are (1) the maximal absorption capacity and (2) the absorption rate of the material. With the exception of the two previously cited studies, little information on these parameters is available in the published literature on iron nanoparticles.

Iron nanoparticles are commonly produced by chemical reduction in liquid phase of a solution of Fe^{2+} or Fe^{3+} by a borohydride reducing solution [11,24]. This method has important advantages such as safety and simple experimental procedure, even though it remains relatively expensive and not environmental-friendly [11]. Suspended in the mother solution, however, the synthesized particles tend to form large aggregates, which can adversely affect their scavenging performance [11]. To avoid this unwanted aggregation, stabilization of zero-valent iron nanoparticles can be realized through surface modification and/or creating a network that separates the nanoparticles [11,25]. Among stabilizers, organic

or inorganic solids such as supports or "vehicles" for stabilizing and delivering iron nanoparticles are frequently used. Several authors have attempted to anchor iron nanoparticles on solid supports such as zeolites [26–28], graphene [19], active carbons [19] or nanoclays [29–32]. This strategy provides several advantages: the aggregation of zerovalent iron nanoparticles is suppressed, the particles can be protected from oxidation and they can be more easily dispersed in a polymer matrix for further application.

The oxidation mechanism of nano-Fe^0 has been largely investigated because Fe^0-based treatment primarily depends on this iron oxidation kinetics [33–36]. All these studies confirmed, using microscopic and spectroscopic techniques, that nano-Fe^0 particles in aqueous environments consists mainly of an inner core of Fe^0 covered by a thin surface layer of iron oxide. This core-shell structure has important implications in terms of nano-Fe^0 reactivity that could be either beneficial for contaminant removal [33] or a drawback when O_2 scavenging properties are sought. Indeed, the oxide layer constitutes a diffusion-limiting layer for O_2 that increases the resistance to oxidation [29] and limits O_2 consumption by the metal core. It is therefore necessary to deepen the understanding of the mechanism of O_2 absorption of such materials and especially of their kinetics to enable the rational development of nano-Fe^0 composites as O_2 scavenging additives.

The objective of this study is therefore to study the essential key parameters, oxygen absorption capacity and absorption rate of iron-based nanoparticles supported on montmorillonite (MMT-Fe) prepared via chemical reduction. The synthetized materials were thoroughly characterized by X-ray Diffraction, HR-TEM, STEM-EDS and ^{57}Fe Mössbauer spectroscopy to get detailed information on their composition and structure, which could be correlated to the oxygen absorption properties. Based on these findings, a semi-mechanistic mathematical model of the O_2 absorption mechanism of MMT-Fe is proposed.

2. Materials and Methods

2.1. Materials

High purity reagents, including ethanol (99%), NaOH (32% aqueous solution), $FeCl_3.6H_2O$ (98%) and sodium borohydride ($NaBH_4$) were purchased from Sigma-Aldrich and used as received. The oganoclay Cloisite 20A (MMT) based on natural montmorillonite modified by dimethyl-ditallow quaternary ammonium salt, characterized by a cation exchange capacity (CEC) of 95 meq/g and d-spacing d_{001} equal to 2.65 nm, was purchased from BYK (Additives & Instruments, Wesel, Germany). The organic modification is necessary for the further dispersion of MMT in a polymer matrix for application in food packaging. Distilled and demineralized water was used throughout these experiments.

2.2. Methods

2.2.1. Preparation of Montmorillonite supported zero valent iron nanoparticles

Zerovalent iron nanoparticles supported on montmorillonite (MMT-Fe) were prepared by reducing the ferric iron (III) with sodium borohydride according to the method adapted from Wang and Zhang [37]. In each batch, 10.13 g of $FeCl_3 \cdot 6H_2O$ were dissolved in a 500 ml solution of deionized water and absolute ethanol in volumetric ratio 1:4. 10.5 g of MMT were added to the $FeCl_3$ solution and the suspension was stirred for 40 h at room temperature.

The iron reducing solution was prepared by dissolving 7.5 g of $NaBH_4$ in 500 ml of an aqueous NaOH solution (475 ml of deionized water and 25 ml of 32% NaOH) and stirred for 16 h for H_2 removal. Dissociating sodium borohydride in a basic solution prevents the production of hydrogen [38]. The MMT-$FeCl_3$·suspension and the $NaBH_4$ solution were air purged by argon bubbling for 2 hours.

250 mL of the $NaBH_4$ solution were added dropwise to the MMT-$FeCl_3$ suspension (B/Fe mole ratio of 4:1) under vigorous stirring (400 rpm). Borohydride reduces Fe^{+3} to Fe^0 according to the following reaction:

$$Fe(H_2O)_6^{3+} + 3BH_4^- + 3H_2O \rightarrow Fe^0\downarrow + 3B(OH)_3 + 10.5H_2$$

Eq. 1

After the addition of $NaBH_4$, the suspension turned black, indicating the reduction of ferric iron. All the experiments were carried out at room temperature under argon flux to eliminate oxygen from the reaction vessel, while maintaining stirring speed constant.

After at least three steps of washing in absolute ethanol (99%), the obtained MMT-Fe was dried in flowing argon for 24 h at room temperature and stored in anoxic conditions. The samples were stored in sealed plastic tubes (centrifuge tube) filled with argon that are themselves stored in hermetic glass storage jars filled with argon and equipped with hermetic airtight seal made of a rubber material. Commercial oxygen scavengers, ATCO® LH-100, provided by Standa laboratory (France) were added in the jar. The operation takes place in a glove box under argon flux (inert gas).

Three different MMT-Fe samples were considered for this study:

- "Wet" MMT-Fe: sample obtained after washing, before the drying step, to evaluate the direct impact of reduction on the physico-chemical state of the iron species;
- "Dried" MMT-Fe: washed and dried sample, to investigate the effect of drying;
- "Stored" MMT-Fe: washed and dried sample stored for 40 days in anoxia, in order to investigate the impact of storage on a possible loss of reactivity.

Iron nanoparticles without MMT support (nano-Fe) were also synthetized using the same protocol without clay.

2.2.2. Characterization methods

ICP-OES. Elemental analysis was performed using an Agilent 700 Series ICP-OES (Inductively Coupled Plasma Optical Emission Spectrometry) spectrometer. Before analysis, MMT and MMT-Fe were dried in an oven at 105 ° C for 24 h. Then samples were mineralised according to the standard protocols NF X31-147 and ISO 14869-1 [39] [40] using fluoro-nitro perchloric etching.

Transmission Electron Microscopy (TEM). Samples for TEM analysis were prepared by depositing a drop of sonicated MMT-Fe or nano-Fe suspension in ethanol on a holey carbon film supported by a 300-mesh copper TEM grid. The structural morphology of iron particles were then analyzed using a JEOL 2200FS transmission electron microscope equipped with STEM-EDS analysis system, operating at 200 kV (JEOL Ltd., Tokyo, Japan) with a

structural resolution of 0.18 nm and a spot size of 0.2 nm. STEM-EDX mapping was performed using a probe size of 1.5 nm and X-rays measured with a silicon drift detector (100 mm^2, Oxford).

Image J Software was used for analysing size distribution of MMT-Fe and nano-Fe particles. About 5 images of a same magnitude (100 and 200 nm) were analysed corresponding to a total of approximately 300 iron particles per type of sample and magnitude.

X-ray diffraction (XRD). Dried MMT-Fe nanoparticles were mounted on a silica holder covered with Kapton film and analyzed using an X'Pert PRO MPD (Multi-Purpose Diffractometer) equipped with the Cu Kα radiation (λ = 1.5418 Å) and operated at 40 kV and 40 mA current. Continuous scans from 5 to 70° 2θ were obtained at a scan rate of 0.012° 2θ min^{-1}.

^{57}Fe Mössbauer spectroscopy. ^{57}Fe Mössbauer spectroscopy was used to obtain information on iron speciation. 40 to 200 mg of wet or dried samples were mounted in a 2 cm^2 holder. Whit the air-sensitive samples, the holder was sealed in argon using Kapton® and aluminum laminated films to avoid air exposure. Mössbauer spectra were measured at variable temperatures between 5 and 300 K in a helium flow cryostat (SHI-850 Series from Janis, USA). The Mössbauer spectrometer (Wissel, Germany) was operated in the transmission mode with a ^{57}Co: Rh source at room temperature. The velocity driver was operated in the constant acceleration mode with a triangular velocity waveform. The velocity scale was calibrated with the magnetically split sextet of a high-purity α-Fe foil at room temperature. The spectra were fitted to appropriate combinations of Lorentzian profiles representing quadrupole doublets, sextets or octets by least-squares methods using the program PC-Mos II [41]. This software is implemented with a specific fitting routine that allows the simultaneous refinement of selected fitting parameters on the whole series of spectra. In this case, only the relative resonance areas were left free to vary independently in each spectrum, whereas the

hyperfine parameters are commonly optimized in the whole series of spectra. In this way, unique spectral parameters such as the hyperfine field (H) quadrupole splitting (Δ), the isomer shift (δ), and the line width at half-maximum (Γ) of the different spectral components were determined for the whole series. These parameters are reported in Table 1. Isomer shifts are given relative to α-Fe at room temperature.

Oxygen absorption measurement.

Oxygen scavenging capacity of synthetized MMT-Fe nanoparticles was determined by measuring the oxygen content as a function of time in the headspace of a tightly closed reactor where a given mass of sample was previously deposited. In this case, 1 to 2 g of sample were placed inside the gas-tight reactor containing 10 mL of pure water at the bottom to maintain a saturated relative humidity (RH). Each sample was measured 5 times. The reactor was closed and placed in a temperature-controlled oven (20°C +/- 1°C).

The headspace oxygen partial pressure was determined using non-invasive optical oxygen sensors (Presens Precision Sensing- GmbH Neuburg; Germany) connected to an oxygen measuring device with a limit of detection at 0.03% and an accuracy of 0.4% O_2 at 20.9% O_2. When the scavenger has absorbed all the O_2 in headspace (partial pressure drop up to 0% in the reactor), a new absorption cycle is realized. To do that, the reactor is reopened to reset the O_2 to 21% and then closed to continue the absorption process. This is done until the scavenger is saturated, *i.e.*, when no more O_2 consumption is detected (constant O_2 partial pressure in headspace). The mass of absorbed O_2 (in g per g of iron) is calculated from headspace-O_2 depletion curve using the approximation of perfect gas law. Oxygen absorption measurements were carried out on all synthetised MMT-Fe samples.

Statistics. Statistical tests were performed by using R software for statistical computing (R, 2014). One way ANOVA was performed to verify if the variance of the data sets was statistically different or not. Comparisons between the compositions were performed by

pairwise comparisons using Tukey's test. Different letters were used to denote significant difference between data sets (level of significance alpha = 0.05, unless stated).

Mathematical modelling and parameters estimation.

In the presence of air and moisture, the oxidation of iron is classically described by the following reaction steps:

$$Fe + \frac{1}{2}O_2 + H_2O \rightarrow Fe(OH)_2 \quad \text{Eq. 2}$$

$$Fe(OH)_2 + \frac{1}{4}O_2 + \frac{1}{2}H_2O \rightarrow Fe(OH)_3 \quad \text{Eq. 3}$$

Absorption of oxygen was thus modelled using two alternative models based on second-order kinetics laws: in a first approach, the two reaction steps (Eqs. 2-3) was reduced to a single chemical reaction by assimilating oxidizable species of iron, *i.e.*, Fe^0 and $Fe(OH)_2$, to a single virtual species $\overline{Fe}$.

$$\overline{Fe} \xrightarrow{\text{oxidation}} Fe(OH)_3 \quad \text{Eq. 4}$$

The absorption kinetic was then depicted by an order 2 kinetic, as O_2 absorption depends on both scavenger and O_2 concentrations. As a simplification, partial orders were set to 1, leading to the following system of ODEs:

$$\frac{dn_{O_2}}{dt} = -k\, n\, n_{O_2} n_{\overline{Fe}} \quad \text{Eq. 5}$$
$$\frac{dn_{\overline{Fe}}}{dt} = -k\, n_{O_2} n_{\overline{Fe}}$$

where n_{O_2} and $n_{\overline{Fe}}$ are the number of mole (mol) of O_2 and oxidizable iron respectively, n is the apparent stoichiometric coefficient (mole O_2 consumed per mole Fe oxidized) and k is the kinetic coefficient ($s^{-1}.mol^{-1}$).

In a second approach, a more precise model was considered by taking into account species Fe^0 and $Fe(OH)_2$ independently. Additionnally, it assumed that iron particles had a core-shell structure, where totally oxidized iron, $Fe(OH)_3$, is located in the shell, Fe^0 in the core and $Fe(OH)_2$ in an intermediate zone. Oxidation of Fe^0 and $Fe(OH)_2$ were considered independent and still following second order kinetics, the model for absorption becomes:

$$\frac{dn_{O_2}}{dt} = -k_1\, n_1\, n_{O_2} n_{Fe} - k_2\, n_2\, n_{O_2} n_{Fe(OH)_2}$$
$$\frac{dn_{Fe}}{dt} = -k_1 n_{O_2} n_{Fe} \qquad \text{Eq. 6}$$
$$\frac{dn_{Fe(OH)_2}}{dt} = -k_2 n_{O_2} n_{Fe(OH)_2}$$

where n_{O_2}, n_{Fe} and $n_{Fe(OH)_2}$ are the number of mole (mol) of O_2, Fe and $Fe(OH)_2$, n_1 and n_2 the apparent stoichiometric coefficients for oxidation of Fe and $Fe(OH)_2$ by O_2, and k_1 and k_2 the kinetic coefficients ($s^{-1}.mol^{-1}$) for oxidation of Fe and $Fe(OH)_2$, respectively.

Numerical simulation of the above ODEs systems were perfomed using Matlab®. Apparent stoichiometric coefficients and kinetic coefficients are specific to the scavenger used. They were estimated by using the Matlab function 'lsqnonlin' with Levenberg-Marquardt method, based on the minimization of the sum of squared error between experimental and predicted data.

3. Results and discussion

3.1. Chemical and structural characterization of the MMT-Fe nanoparticles

ICP-OES analyses reavealed an average iron contents of 0.23±0.1, 0.22±0.01 and 0.02±0.008 g per gram of dry powder for "Wet" MMT-Fe, "Dried" MMT-Fe and pristine MMT, respectively. Since the iron content of MMT is about an order of magnitude lower than that of MMT-Fe, it will be considered as negligible in the following. As expected, there was no significant difference between iron content in "Wet" and "Dried" MMT-Fe.

The XRD patterns of all MMT-Fe samples show mainly the Bragg diffraction peaks of pristine MMT. The d-spacing (d_{001}=1.30 nm) of modified montmorillonite does not change after the synthesis of the iron nanoparticles, indicating that its structure is not modified and that no iron ions are intercalated in the interlayer spacing. This indicates that iron nanoparticles are only on the external surface of MMT. "Wet", "Dried" and "Stored" Fe-MMT display in addition some weak defined peaks that can be be attributed to iron oxides (likely γ-Fe_2O_3 and/or Fe_3O_4) (Fig. 1). Due to similar lattice constants, the two oxides (γ-

Fe_2O_3 and Fe_3O_4) cannot be distinguished from such weak signals [33,42]. No signal from zerovalent iron species could be detected in any XRD pattern. This clearly shows that any zerovalent iron species contained in MMT-Fe samples is nanosized and/or in the amorphous state.

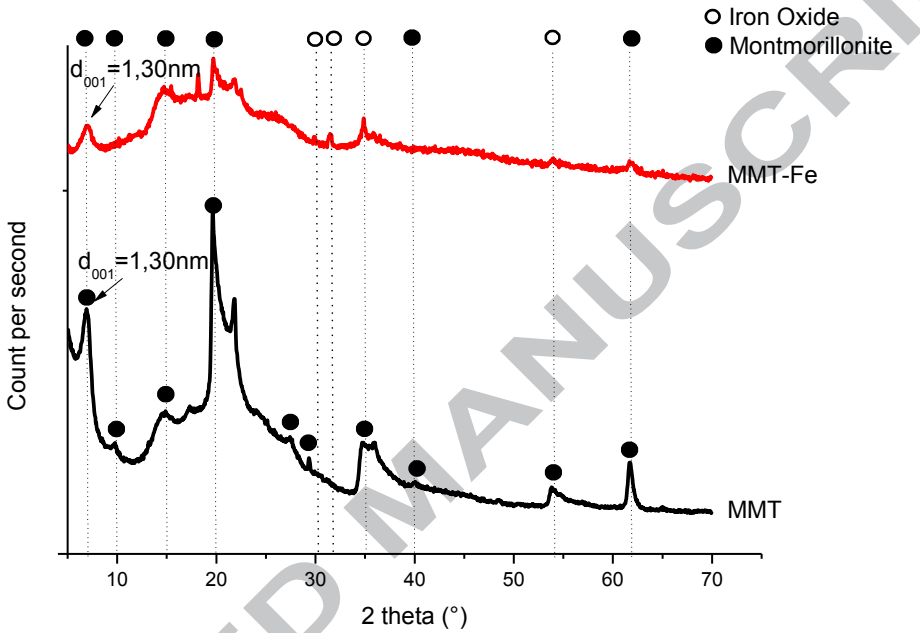

Figure 1: Typical XRD patterns obtained for (a) MMT an (b) Dried MMT-Fe particles.

^{57}Fe Mössbauer spectra were collected for all iron precursors (not shown) confirming the Fe^{3+} state of iron in $FeCl_3$ and the presence of a mixture of Fe^{2+} (16%) and Fe^{3+} (84%) in pristine MMT. Fig. 2 shows the typical spectra at 5 K of MMT-Fe and of the nano-Fe reference. Both samples show very complex but quite similar spectra, which can be deconvoluted into at least four spectral components:

(i) Most of the iron (30-60%) is represented by a broadened sextet characterised by an isomer shifts of 0.07 mm/s and an average hyperfine field of 30.7 T. Such parameters, significantly different from those of α-Fe metal, support the formation of amorphous iron borides, in agreement with several previous reports indicating that the reduction of iron cations by borohydride anion can lead to the formation of amorphous $Fe_{1-x}B_x$ [43–45]. This result is supported by the detection of boron in the sample even after several washing steps.

Correlations were established in the literature between the hyperfine parameters (magnetic field and isomer shift) and the boron content (x) of the formed alloy. In some case x can be as high as 0.4 [46]. According to Kemény *et al.*, the $Fe_{1-x}B_x$ species in our MMT-Fe samples contain less than 15 % of boron ($x < 0.15$) since the hyperfine field is around 28 T at room temperature [47]. In the nano-Fe reference, conversely, they contain more than 25 % of boron. It is worth noting that such species could not be detected by XRD due to their amorphous character.

(ii) Two different spectral contributions, a magnetic octet and a quadrupole split component, can be attributed to Fe^{2+} based on their high isomer shift (1.21 mm/s). The presence of an important fraction of divalent iron suggests either an incomplete reduction of iron cations or a fast re-oxidation of the Fe-B nanoparticles. Even though the exact nature of these species is not known, their formation is not related to the clay support since they are also observed in the reference sample nano-Fe.

(iii) An additional weak sextet with an hyperfine field of 49 T and an isomer shift of 0.38 mm/s can be attributed to iron oxides such as Fe_2O_3. Since this sextet collapses at room temperature into a doublet with an isomer shift of 0.40 mm/s it can be concluded that this oxide consists of very small and/or amorphous particles undergoing superparamagnetic relaxation. In the nano-Fe sample, it represents less than 4% of the total reference area. Similar components have been reported in the case of sodium borohydride reduction of ferrous or ferric ions [44,46,48,49]. XPS data on such samples showed that the ratio between Fe^0 and Fe^{3+} depends on the sample's preparation conditions and history [44].

(iv) Finally, the typical magnetic sextet of α-Fe was detected only in the clay-free nano-Fe reference. Indeed, α-Fe was previously found in similar materials also by Linderoth and Morup, who showed that boron free α-Fe is favoured by a low B/Fe ratio [46].

Table 1. ^{57}Fe Mössbauer parameters at 5 K for "Wet" MMT-Fe and Nano-Fe

Sample	Comp.	IS (mm/s)	QS (mm/s)	LW (mm/s)	H (Tesla)	Area (%)
MMT-Fe	Fe^{2+} magn	1.21	-2.78	1.72	15.0	27
	$Fe_{1-x}B_x$	0.08	-0.03	0.47	30.8	62
	Fe^{3+} oxide	0.37	-0.12	0.60	49.0	3
	Fe^{2+} para	1.25	3.03	0.66	-	8
Nano-Fe	$Fe_{1-x}B_x$	0.34(4)	0.00	2.7(2)	25.2(2)	37(3)
	α-Fe	0.11(2)	0.00	0.46(7)	34.7(2)	5(1)
	Fe^{2+} para	1.32(1)	2.80(2)	0.77(4)	-	17(1)
	Fe^{2+} magn	1.31(5)	-2.8(2)	2.0(2)	11.7(6)	38(3)
	Fe^{3+} oxide	0.48(5)	0.00	1.0(5)	51.8(7)	3(1)

These results show that, contrarily to the simplified situation usually given in litterature referring to ZVI (zero valent iron) or iron NPs (nanoparticles), the iron species formed during chemical reduction using $NaBH_4$ of trivalent iron solutions are very complex and may contain many amorphous or nanosized species including Fe metal, iron borides, as well as oxidic species containing Fe^{2+} and Fe^{3+} [26].

It is worth noting that pristine MMT also contained a minor amount of iron (summing up to less than 20% of the total iron in MMT-Fe). The Mössbauer spectrum of the pristine clay (not shown) can be deconvoluted into two quadrupole doublets, representing divalent and trivalent iron. These components are not clearly detectable in the the spectra of MMT-Fe most probably because this iron has also reacted during the synthesis and is now included in some of the new spectral components. A complete ion exchange during reaction cannot be excluded, as described in [50].

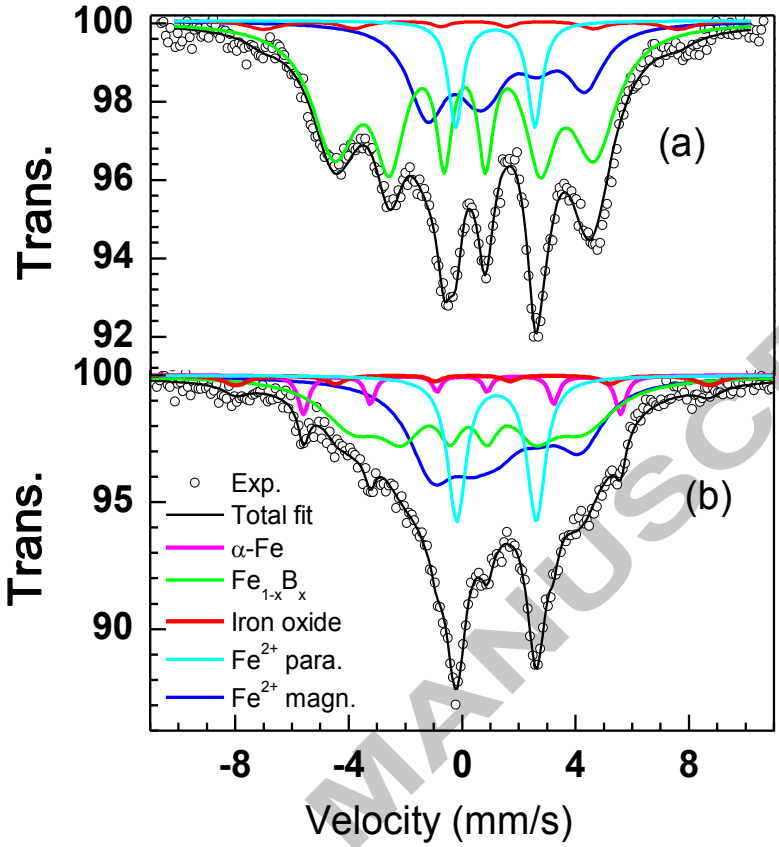

Figure 2: Typical Mössbauer spectra of (a) Wet MMT-Fe and (b) nano-Fe samples at 5°K.

Fig. 3 shows the TEM images of pure nano-Fe and MMT-Fe. The clays-supported iron particles are mostly aggregates of small spherical nanoparticles with a mean diameter of 6 to 20 nm. The high resolution TEM (HR-TEM) picture of oxidized MMT-Fe sample clearly shows the typical core-shell structure of zero-valent iron nanoparticles, with a bright iron oxide shell coating the dark iron core [29,33,34,51]. It is worth noting that the oxide shells have an almost constant thickness of 3 to 5 nm, similar to that observed by [29].

The particle size distribution (Fig. 3c) obtained by sampling more than 300 particles in the low magnification TEM images of MMT-Fe (Fig. 3b) gives a mean diameter of 57 ± 17 nm. Much larger aggregates are obtained for the reference Nano-Fe sample (Fig. 3e) than for MMT-Fe (Fig. 3d), confirming the role of MMT in helping dispersion and limiting aggregation. However, this agglomeration shows that iron particles are not really anchored on the surface of MMT, but simply deposited on it.

In a previous study on Fe-bentonite systems, Üzüm et al. [32] obtained large particles with a mean diameter in the range of 10–60 nm, partly agglomerated despite the clay support. On the other hand, Mingde Fan et al. [29] observed only well-dispersed spherical particles with a mean diameter of 55±11 nm in their study of iron dispersed on sodium montmorillonite, synthetized in conditions similar to the present work with borohydride to iron molar ratio of 4:1, but in the absence of NaOH. This confirms that not only the borohydride to iron molar ratio, but also the solvent and the presence of NaOH influence the structure and morphology of the synthetized Fe nanoparticles.

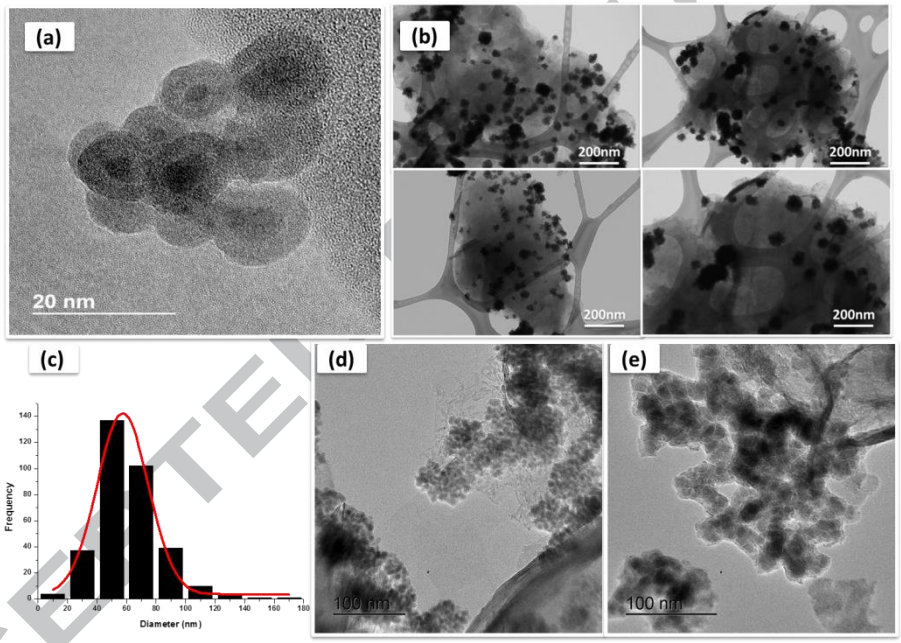

Figure 3: Overview of iron MMT-Fe and nano-Fe particles: HR-TEM (a), low-magnification TEM images of MMT-Fe particles (b & d) and Nano-Fe particles (e) and particle size distribution in MMT-Fe sample (c)

The elemental mapping of Fe, Si, and O made by STEM-EDS on MMT-Fe samples is shown in Fig. 4-A. EDS spectra with significant peaks of O (43.81 w/w %) Fe (28.4%) Si (19.12%) Al (7.38%) Mg (1.01%) and Cl (0.27%) confirmed the presence of iron (Fe^0) and elemental elements related to iron oxides (O), MMT (Si, Al, Mg). C corresponded to the support used for doing the analysis and Cl to residues from the synthesis using $FeCl_3$ as precursor. No clear signal of boron is visible in the STEM-EDS spectrum shown in Fig. 4-A. The low

sensitivity of EDS to light elements and the very small amount of boron expected in the sample, however, do not exclude its presence in the synthetized powder.

Similar elemental mapping was obtained for nano-Fe, with the exception that now the signal of boron, even though still very weak, is clearly visible, whereas those of Si, Al and Mg, which come from MMT support, are absent (Fig. 4-B).

In summary, the reduction of iron by $NaBH_4$ in basic conditions leads to relatively small particles of about 57 nm in diameter dispersed on the MMT support. Such particles are mainly aggregates of amorphous iron boride nanoparticles with an average size of 6-20 nm exhibiting, after oxidation, a typical core-shell structure.

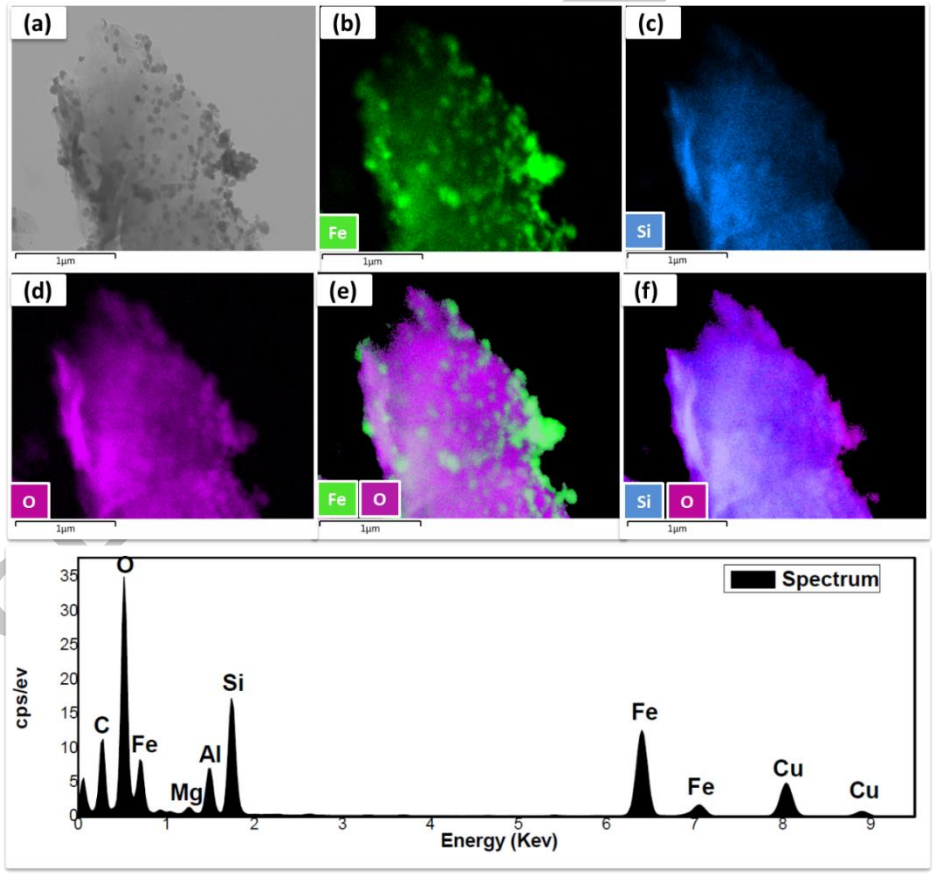

-A-

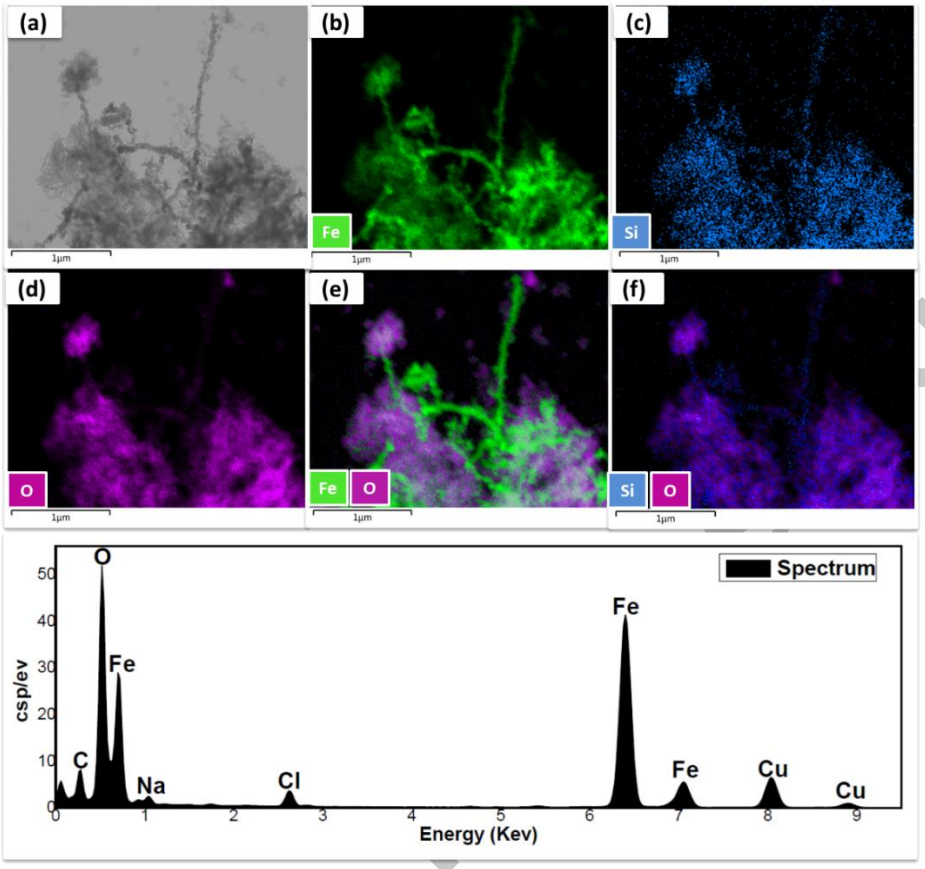

- B-

Figure 4: STEM-EDS elemental analysis mapping of MMT-Fe (A) and nano-Fe (B). (a) STEM. (b) Fe map. (c) Si map. (d) O map. (e) Fe + O map. (f) Si + O map. The average EDS spectra are shown at the bottom.

3.2. *In Situ* measurements of O_2 absorption capacity

The absorption capacity was measured for "Wet", "Dried", and "Stored" MMT-Fe in a water vapor saturated atmosphere. Under these conditions, the oxidation of 1 mole of iron by oxygen consumes 1.5 mole of water, *i.e.*, 0.5 g of water per g of iron [52]. It was assumed that the iron boride particles oxidise as Fe^0 and that boron does not participate into in the reaction. Under this assumption, 1 g of iron can absorb 0.394 g of oxygen, corresponding to 300 cc at room temperature.

Fig. 5 contains examples of headspace-O_2 depletion curve and corresponding O_2 absorption curves (calculated from the headspace-O_2 depletion curve in the perfect gas law approximation) for "Wet" and "Dried" MMT-Fe.

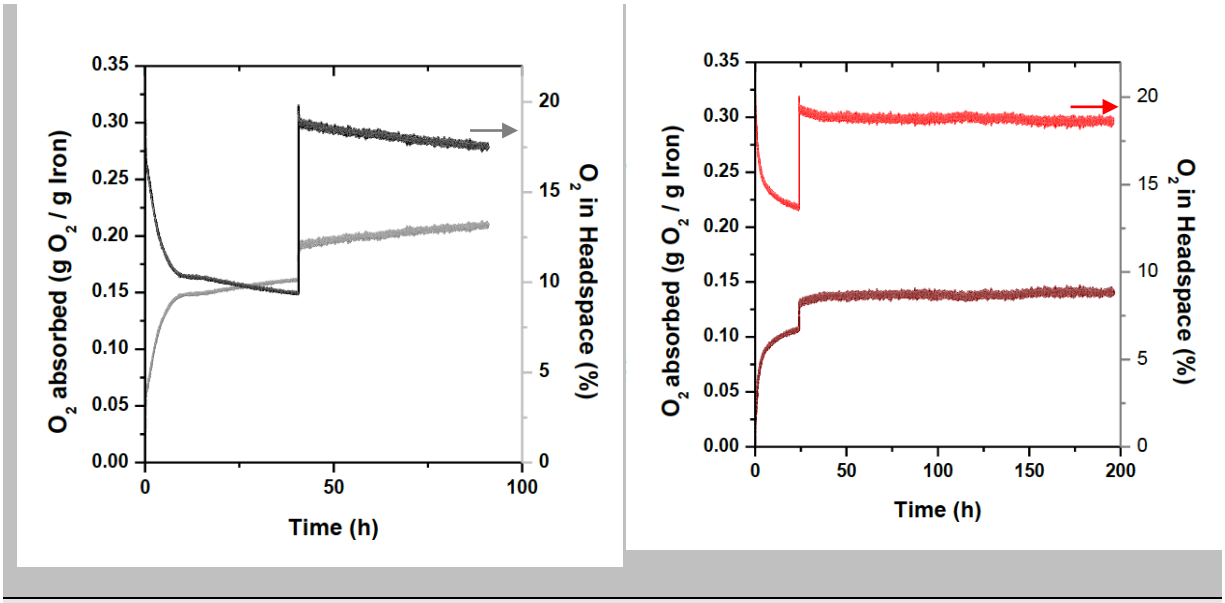

Figure 5: Examples of experimental headspace-O_2 depletion curves (right y-axis) and corresponding O_2 absorption curves (left y-axis) for A) Wet MMT-Fe and B) Dried MMT-Fe

The absorption patterns of "wet", "dried" and "stored" MMT-Fe, shown in Fig. 6, are sensibly different. Firstly of all, "wet" MMT-Fe absorbs more quickly at the beginning (first 30 min) than the "dried" and "stored" samples. Then secondly, the absorption rate of "stored" MMT-Fe is lower than that of "dried" MMT-Fe. Finally, the high (very high for "wet" MMT-Fe) initial absorption rates of the three samples at the beginning of the process decrease rapidly and continuously after the first 30 min.

After about 72 h of the absorption process, the O_2 absorption capacity of "Wet" MMT-Fe (0.20 ± 0.01 g O_2 per g of iron) levels off at a much higher value than that of "Dried" and "Stored" samples (0.14 ± 0.03 and 0.09 ± 0.00 g O_2 per g of iron, respectively). It was checked that pristine MMT does not contribute to the O_2 absorption (results not shown). In all cases, the absorption capacity is below the maximum theoretical value (0.4 g of O_2 per g of iron) for all the systems. This could be easily explained considering that iron in MMT-Fe is not only zerovalent, but that about a third of it is divalent. Moreover, the core-shell structure of the iron nanoparticle hinders the diffusion of oxygen to the zerovalent core, limiting the complete oxidation process. It is worth noting that the absorption capacity of the synthetized MMT-Fe samples, measured after 72h, is relevant for food packaging application. Indeed, to absorb 21 mL of oxygen (which corresponds to a realistic headspace volume of 100 mL), 0.15 g of pure iron is necessary, i.e. 0.75 g of "Wet" MMT-Fe if used as O_2 scavenger sachet. In other words, 1 g of MMT-Fe powder absorbs about 28 mL of O_2 which is in the same order of magnitude than capacity usually obtained for other conventional scavenger systems in food packaging, such as for example, 6.72 ml O_2 per g absorber for alpha-tocopherol based system [53], 43 ml O_2 per g absorber for iron powder [54] or 61 mL per g absorber for pyrogallol coated onto a modified LDPE film [55].

The higher initial oxygen absorption rate of "wet" MMT-Fe compared to the "dried" and "stored" samples can be explained either by considering the presence of water in contact with the iron particles in the "wet" sample, which might directly influence the oxidation rate, or by the observed partial oxidation of iron during the drying and storage processes (*vide infra*), which inertises the most active portion of the active iron (most probably at the surface of the nanoparticles) already before the oxygen absorption test.

The possible effect of the direct presence of water on the reactivity was tested by measuring the initial slopes of the absorption curves of a MMT-Fe sample dispersed in a 1:1 vol. solution of ethanol and water in the time ranges 0-3, 0-18 and 0-30 min (Fig. 7). The slopes of "dispersed" MMT-Fe were always higher than those of the other samples, confirming that the hydration level of the system also influences the kinetics of the oxidation.

In summary, "dried" and "stored" MMT-Fe absorb oxygen more slowly and in lower amounts than "wet" MMT-Fe. Drying and storage influence the absorption kinetics because "dried" and "stored" MMT-Fe are more oxidized than the "wet" sample, but also the presence of water in direct contact with the particles influences the reaction rate. This impact, however, remains low enough to conclude that MMT-Fe powders can be stored without impairing too much their absorption capacity in the long time.

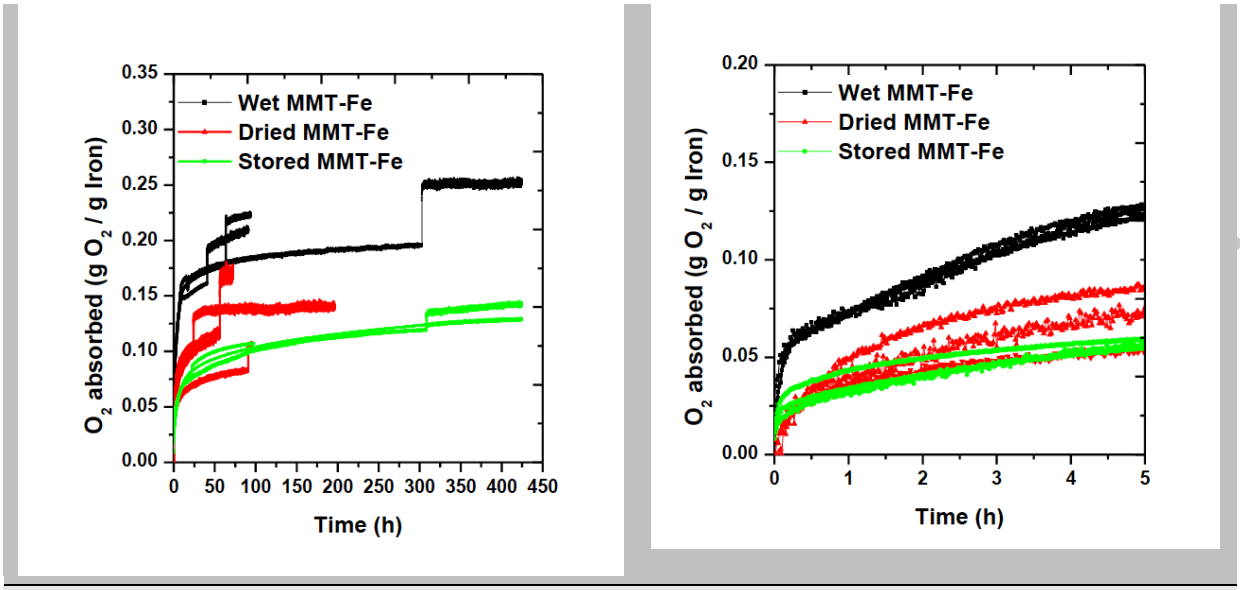

Figure 6: Comparison of oxygen absorption curves for Wet MMT-Fe, Dried MMT-Fe and Stored MMT-Fe (A) full curve and (B) zoom on the first 5 hours

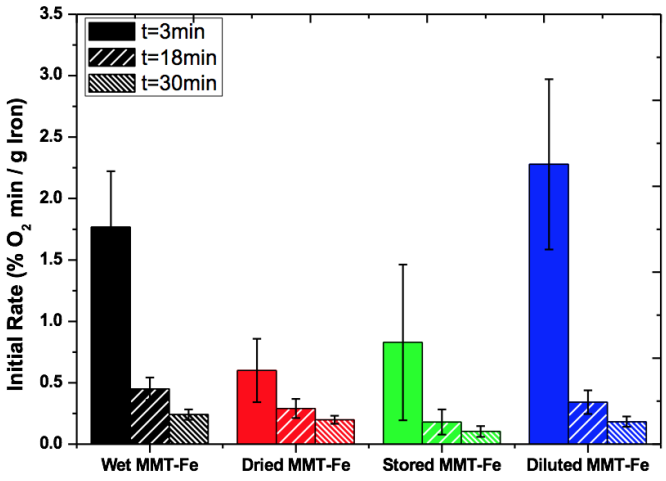

Figure 7: Initial slopes of the absorption curves for "wet", "dried", "stored" and "dispersed" MMT-Fe.

3.3. In situ Mössbauer study of O_2 absorption kinetics

The kinetics of oxygen absorption of MMT-Fe was monitored by Mössbauer spectroscopy going from the wet slurry to "dried" MMT-Fe, and after exposure of the latter to ambient atmosphere for increasing periods of time (Fig. 8). "Dried" MMT-Fe contains a larger amount of Fe^{3+} oxide than the "wet" sample. The fitting model used to fit the spectrum of "wet" MMT-Fe can be applied successfully to all the other spectra keeping all the parameters fixed with the exception of the relative resonance area of the different components. By doing

so, it is possible to follow the evolution of all iron species during air exposure, which is shown in Fig. 9. During exposure to air, the amount of Fe^{+3} increases at the expenses of both zerovalent and divalent iron. The oxidation of "Dried" MMT-Fe shows a 2 stages mechanism with a high activity during the first minutes (up to 30 min) analysis of Fig. 6. These two stages are correlated with iron species activities since in the first stage, mainly Fe^{2+} undergoes oxidation while the second step correlates well with the oxidation of Fe^{0}.

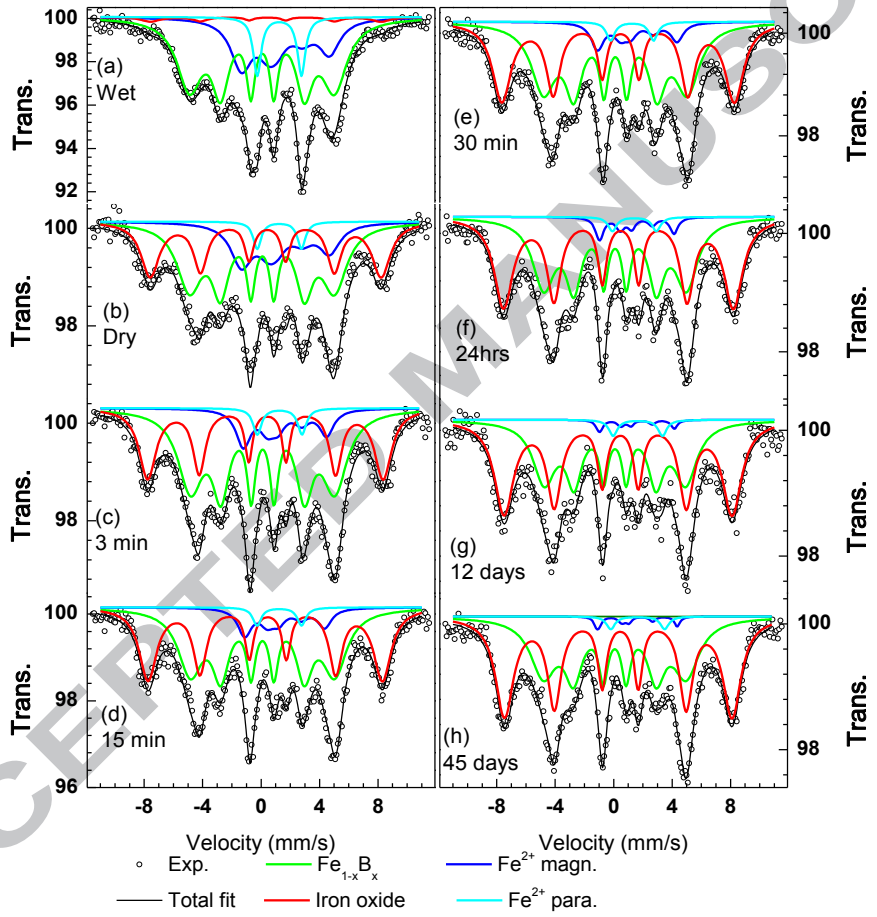

Figure 8: Mössbauer spectra at 5 K of wet (a), dried (b) MMT-Fe material before any air exposure. Spectra (c) to (h) were collected after air exposure for the indicated time.

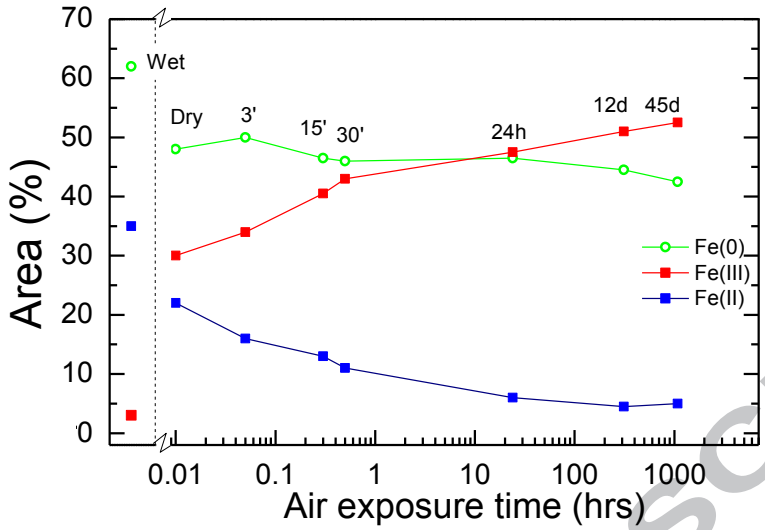

Figure 9: Evaluation of iron species after air exposure. The initial wet composition is shown for comparison. (Note the logarithmic x-axis).

3.4. Mathematical modelling of O_2 absorption

In order to predict the dynamic of O_2 scavenging, both the global model (Eq. 4) and the 2-species model (Eq. 5) were compared to experimental data for "Wet" and "Dried" MMT-Fe (5 replicates each). Parameter estimation and comparison between experimental and simulated data were performed on the first cycle of O_2 absorption only. The initial amounts of Fe^0, $Fe(OH)_2$ and $\overline{Fe}$ were taken from the Mössbauer measurements (Figure 2).

The experimental curves of O_2 absorption (Figure 5) showed dynamics characteristic of kinetics of order two or greater as proved by the non-liear curve obtained by plotting Log [O_2] as a function of time. This was confirmed by the simulations of the global model which had always higher RMSE values than the 2-species model: the global model led to RMSE values of 0.50 ± 0.16 %O_2 and 0.34 ± 0.08 %O_2 for wet and dried MMT-Fe respectively, compared to 0.21 ± 0.09 %O_2 and 0.11 ± 0.03 %O_2 for wet and dried MMT-Fe by using the 2 species model. Additionally, the global model was never able to catch the slow decreasing dynamic at long times.

The global model was then given up for the 2-species model. The 2-species model correctly reproduced the observed kinetics for both "Wet" and "Dried" samples. Estimated parameters

(mean ± standard deviation) are summarized in Table 2. The 2-species model better fitted the O_2 absorption curves obtained for dried samples than for wet samples. Figure 10 illustrates the fit quality for a dried MMT-Fe replicate. The lower fitting quality for wet MMT-Fe can be explained by the presence of residual solvent which might either reduce the aggregation of MMT platelets or modify the diffusion of O_2 from atmosphere to the Fe nanoparticles, both impacting the O_2 absorption and being not taken into account in the model. The additional direct oxidation of Fe^0 by water, which may occur in the absence of oxygen based on the respective standard redox potentials of water and iron but which is expected to be relatively slow in non-acidic conditions, might also influence the observed kinetics.

Table 2: Estimated parameters for 2-species model on wet and dried MMT-Fe. Mean ± standard deviation were calculated on 6 replicates.

	k_1 $(s^{-1}.mol^{-1})$	n_1 $(mol.mol^{-1})$	k_2 $(s^{-1}.mol^{-1})$	n_2 $(mol.mol^{-1})$	RMSE (% of O_2)
wet MMT-Fe	$2.9\ 10^{-6} \pm 3.5\ 10^{-6}$	0.47 ± 0.49	$1.8\ 10^{-4} \pm 2.4\ 10^{-4}$	0.39 ± 0.20	0.21 ± 0.09
dried MMT-Fe	$2.4\ 10^{-6} \pm 1.7\ 10^{-6}$	0.19 ± 0.07	$3.2\ 10^{-5} \pm 1.25\ 10^{-5}$	0.40 ± 0.13	0.11 ± 0.03

Globally, the estimated kinetic parameters are significantly higher for $Fe(OH)_2$ than for Fe, in accordance with the Mössbauer kinetics (Fig. 9). This 2-species model accurately reproduces both fast and slow dynamics during O_2 absorption for dried MMT-Fe (Figure 10-a). The model also provides the mass of not fully oxidized iron during the absorption cycle (Figure 10-b). It predicted a full oxidation of $Fe(OH)_2$ (no $Fe(OH)_2$ remaining after 5h) while the remaining Fe^0 oxidises slowly. However, this model underestimated the remaining Fe^0 compared to Mössbauer kinetics (Fig. 9). It was due to the strong assumption made in the 2-species model that all the oxidizable iron is fully accessible for oxidation. Indeed, the core-shell structure which is classically reported in the literature [33] and which is observed by HR-TEM in MMT-Fe, causes the Fe^0 core to be passivated by an oxide shell. The 2-species

model is efficient in predicting the O_2 scavenging kinetics of “Wet” and "“Dried” MMT-Fe and can be a candidate for predicting the O_2 scavenging properties in further applications.

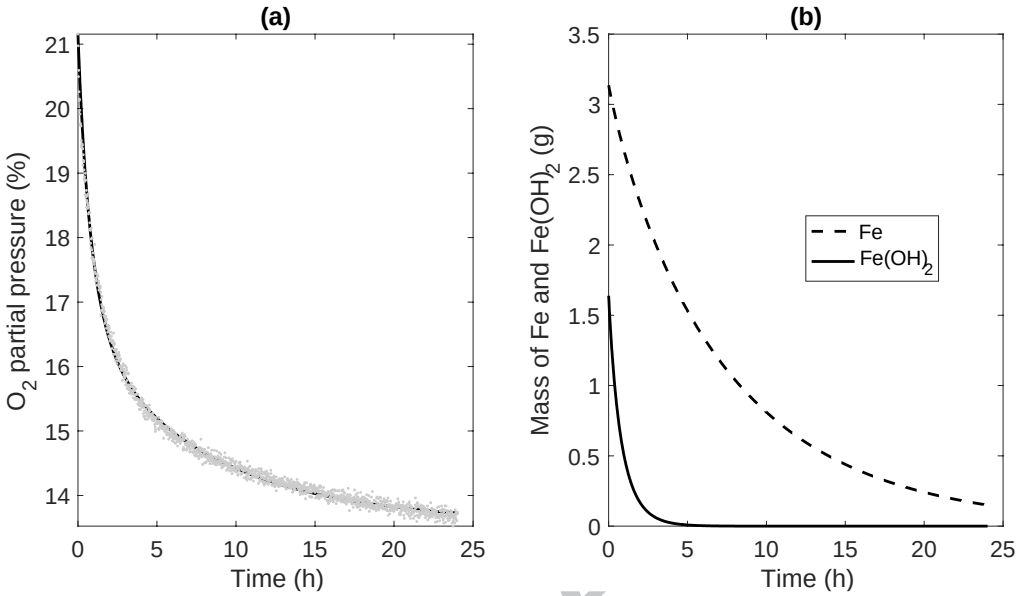

Figure 10: Prediction of O_2 absorption and residual active scavenger for “Dried” MMT-Fe, by using 2-species model (Eq. 5). (a) Comparison of experimental (grey dots) and predicted (black line) data for headspace-O_2 depletion curves. (b) Prediction of Fe (line) and $Fe(OH)_2$ (dashed line) content.

4. Conclusion

The reduction of iron with $NaBH_4$ under basic conditions leads to the formation of amorphous $Fe_{1-x}B_x$ on aggregate particles identified by Mössbauer analysis. These aggregates have a size of about 57 nm and are quite well dispersed on MMT support although not well anchored on it. The Mössbauer kinetics on MMT-Fe confirms that the different iron nanoparticle phases do not oxidize at the same rate. Oxygen absorption was modelled using a second-order kinetic equation. The measured absorption capacity, high absorption rate constant and the two species kinetic model confirm the potential of such tailored absorbers in food packaging. This model and parameters, and the accompanying insight into the functioning of this scavenger, could assist in the formulation of active nanocomposite packaging films.

References

[1] H. Angellier-coussy, V. Guillard, C. Guillaume, N. Gontard, Role of packaging in the

smorgasbord of action for sustainable food consumption, Agro Food Ind. 23 (2013) 15–19.

[2] C. Guillaume, P. Chalier, N. Gontard, Modified atmosphere packaging usingenvironmentally compatible and active food packaging, in: C. E. (Ed.), Environ. Compat. Food Packag., Boca Raton: CRC Press, 2008: pp. 396–418.

[3] T. Cagnon, A. Méry, P. Chalier, C. Guillaume, N. Gontard, Fresh food packaging design: A requirement driven approach applied to strawberries and agro-based materials., Innov. Food Sci. Emerg. Technol. 20 (2013) 288–298. doi:10.1016/j.ifset.2013.05.009.

[4] K. Kaiser, M. Schmid, M. Schlummer, Recycling of Polymer-Based Multilayer Packaging : A Review, (2018). doi:10.3390/recycling3010001.

[5] Y. Cui, S. Kumar, B. Rao Kona, D. van Houcke, Gas barrier properties of polymer/clay nanocomposites, RSC Adv. 5 (2015) 63669–63690. doi:10.1039/C5RA10333A.

[6] G. Choudalakis, a. D. Gotsis, Permeability of polymer/clay nanocomposites: A review, Eur. Polym. J. 45 (2009) 967–984. doi:10.1016/j.eurpolymj.2009.01.027.

[7] S. Dadbin, M. Noferesti, M. Frounchi, Oxygen barrier LDPE/LLDPE/organoclay nano-composite films for food packaging, Macromol. Symp. 274 (2008) 22–27. doi:10.1002/masy.200851404.

[8] J.M. Lagarón, L. Cabedo, D. Cava, J.L. Feijoo, R. Gavara, E. Gimenez, Improving packaged food quality and safety. Part 2: Nanocomposites, Food Addit. Contam. 22 (2005) 994–998. doi:10.1080/02652030500239656.

[9] C. Wolf, H. Angellier-coussy, N. Gontard, F. Doghieri, V. Guillard, How the shape of fi llers a ff ects the barrier properties of polymer / non-porous particles nanocomposites : A review, J. Memb. Sci. 556 (2018) 393–418. doi:10.1016/j.memsci.2018.03.085.

[10] C. Noubactep, S. Caré, R. Crane, Nanoscale metallic iron for environmental remediation: Prospects and limitations, Water. Air. Soil Pollut. 223 (2012) 1363–1382.

doi:10.1007/s11270-011-0951-1.

[11] X. Zhao, W. Liu, Z. Cai, B. Han, T. Qian, D. Zhao, An overview of preparation and applications of stabilized zero-valent iron nanoparticles for soil and groundwater remediation, Water Res. 100 (2016) 245–266. doi:10.1016/j.watres.2016.05.019.

[12] X. Li, D.W. Elliott, W. Zhang, Zero-Valent Iron Nanoparticles for Abatement of Environmental Pollutants: Materials and Engineering Aspects, Crit. Rev. Solid State Mater. Sci. 31 (2006) 111–122. doi:10.1080/10408430601057611.

[13] F. Fu, D.D. Dionysiou, H. Liu, The use of zero-valent iron for groundwater remediation and wastewater treatment: A review, J. Hazard. Mater. 267 (2014) 194–205. doi:10.1016/j.jhazmat.2013.12.062.

[14] M. Diao, M. Yao, Use of zero-valent iron nanoparticles in inactivating microbes, Water Res. 43 (2009) 5243–5251. doi:10.1016/j.watres.2009.08.051.

[15] S. Yang, P. Wu, J. Liu, M. Chen, Z. Ahmed, N. Zhu, Efficient removal of bisphenol A by superoxide radical and singlet oxygen generated from peroxymonosulfate activated with Fe0-montmorillonite, Chem. Eng. J. 350 (2018) 484–495. doi:10.1016/j.cej.2018.04.175.

[16] S. Yang, P. Wu, Q. Ye, W. Li, M. Chen, N. Zhu, Efficient catalytic degradation of bisphenol A by novel Fe0- vermiculite composite in photo-Fenton system: Mechanism and effect of iron oxide shell, Chemosphere. 208 (2018) 335–342. doi:10.1016/j.chemosphere.2018.06.008.

[17] Z. Qu, A. Garfinkel, J.N. Weiss, M. Nivala, Multi-scale modeling in biology: How to bridge the gaps between scales?, Prog. Biophys. Mol. Biol. 107 (2011) 21–31. doi:10.1016/j.pbiomolbio.2011.06.004.

[18] A.K. Gupta, M. Gupta, Synthesis and surface engineering of iron oxide nanoparticles for biomedical applications, Biomaterials. 26 (2005) 3995–4021.

doi:10.1016/j.biomaterials.2004.10.012.

[19] L. Mohammed, H.G. Gomaa, D. Ragab, J. Zhu, Magnetic nanoparticles for environmental and biomedical applications: A review, Particuology. 30 (2017) 1–14. doi:10.1016/j.partic.2016.06.001.

[20] H. Mu, H. Gao, H. Chen, F. Tao, X. Fang, L. Ge, A nanosised oxygen scavenger: Preparation and antioxidant application to roasted sunflower seeds and walnuts, Food Chem. 136 (2013) 245–250. doi:10.1016/j.foodchem.2012.07.121.

[21] M.J. Galotto, S.A. Anfossi, A. Guarda, Oxygen Absorption Kinetics of Sheets and Films Containing a Commercial Iron-based Oxygen Scavenger, FOOD Sci. Technol. Int. 15 (2009) 159–168. doi:10.1177/1082013208106207.

[22] M.A. Busolo, J.M. Lagaron, Oxygen scavenging polyolefin nanocomposite films containing an iron modified kaolinite of interest in active food packaging applications, Innov. Food Sci. Emerg. Technol. 16 (2012) 211–217. doi:10.1016/j.ifset.2012.06.008.

[23] Z. Foltynowicz, A. Bardenshtein, S. Sängerlaub, H. Antvorskov, W. Kozak, Nanoscale, zero valent iron particles for application as oxygen scavenger in food packaging, Food Packag. Shelf Life. 11 (2017) 74–83. doi:10.1016/j.fpsl.2017.01.003.

[24] L. Li, M. Fan, R.C. Brown, J. (Hans) Van Leeuwen, J. Wang, W. Wang, et al., Synthesis, Properties, and Environmental Applications of Nanoscale Iron-Based Materials: A Review, Crit. Rev. Environ. Sci. Technol. 36 (2006) 405–431. doi:10.1080/10643380600620387.

[25] Y.P. Sun, X.Q. Li, W.X. Zhang, H.P. Wang, A method for the preparation of stable dispersion of zero-valent iron nanoparticles, Colloids Surfaces A Physicochem. Eng. Asp. 308 (2007) 60–66. doi:10.1016/j.colsurfa.2007.05.029.

[26] E. Xingu-Contreras, G. García-Rosales, A. Cabral-Prieto, I. García-Sosa, Degradation of methyl orange using iron boride nanoparticles supported in a natural zeolite, Environ.

Nanotechnology, Monit. Manag. 7 (2017) 121–129. doi:10.1016/j.enmm.2016.12.003.

[27] S.A. Kim, S. Kamala-Kannan, K.J. Lee, Y.J. Park, P.J. Shea, W.H. Lee, et al., Removal of Pb(II) from aqueous solution by a zeolite-nanoscale zero-valent iron composite, Chem. Eng. J. 217 (2013) 54–60. doi:10.1016/j.cej.2012.11.097.

[28] Z.X. Chen, X.Y. Jin, Z. Chen, M. Megharaj, R. Naidu, Removal of methyl orange from aqueous solution using bentonite-supported nanoscale zero-valent iron, J. Colloid Interface Sci. 363 (2011) 601–607. doi:10.1016/j.jcis.2011.07.057.

[29] M. Fan, P. Yuan, J. Zhu, T. Chen, A. Yuan, H. He, et al., Core-shell structured iron nanoparticles well dispersed on montmorillonite, J. Magn. Magn. Mater. 321 (2009) 3515–3519. doi:10.1016/j.jmmm.2009.06.060.

[30] S. Bhowmick, S. Chakraborty, P. Mondal, W. Van Renterghem, S. Van den Berghe, G. Roman-Ross, et al., Montmorillonite-supported nanoscale zero-valent iron for removal of arsenic from aqueous solution: Kinetics and mechanism, Chem. Eng. J. 243 (2014) 14–23. doi:10.1016/j.cej.2013.12.049.

[31] T. Shahwan, C. Üzüm, A.E. Eroğlu, I. Lieberwirth, Synthesis and characterization of bentonite/iron nanoparticles and their application as adsorbent of cobalt ions, Appl. Clay Sci. 47 (2010) 257–262. doi:10.1016/j.clay.2009.10.019.

[32] Ç. Üzüm, T. Shahwan, A.E. Eroğlu, K.R. Hallam, T.B. Scott, I. Lieberwirth, Synthesis and characterization of kaolinite-supported zero-valent iron nanoparticles and their application for the removal of aqueous Cu2+ and Co2+ ions, Appl. Clay Sci. 43 (2009) 172–181. doi:10.1016/j.clay.2008.07.030.

[33] N. Kumar, M. Auffan, J. Gattacceca, J. Rose, L. Olivi, D. Borschneck, et al., Molecular insights of oxidation process of iron nanoparticles: Spectroscopic, magnetic, and microscopic evidence, Environ. Sci. Technol. 48 (2014) 13888–13894. doi:10.1021/es503154q.

[34] L. Signorini, L. Pasquini, L. Savini, R. Carboni, F. Boscherini, E. Bonetti, et al., Size-dependent oxidation in iron/iron oxide core-shell nanoparticles, Phys. Rev. B. 68 (2003) 195423.

[35] C. Wang, D.R. Baer, J.E. Amonette, M.H. Engelhard, J. Antony, Y. Qiang, Morphology and electronic structure of the oxide shell on the surface of iron nanoparticles, J. Am. Chem. Soc. 131 (2009) 8824.

[36] Q. Wang, S. Lee, H. Choi, Aging study on the structure of Fe0-nanoparticles: stabilization, characterization, and reactivity, J. Phys. Chem. C. 114 (2010) 2027.

[37] C. Wang, W. Zhang, Synthesizing Nanoscale Iron Particles for Rapid and Complete Dechlorination of TCE and PCBs, Env. Sci Technol. 31 (1997) 2154.

[38] H.I. Schlesinger, H.C. Brown, A.E. Finholt, J.R. Gilbreath, H.R. Hoekstra, E.K. Hyde, Sodium Borohydride, Its Hydrolysis and its Use as a Reducing Agent and in the Generation of Hydrogen, J. Am. Chem. Soc. 75 (1953) 215–219. doi:10.1021/ja01097a057.

[39] NF X31-147, Qualité des sols - Sols, sédiments - Mise en solution totale par attaque acide, (1996) 14.

[40] NF ISO 14869-1, Qualité du sol - Mise en solution pour la détermination des teneurs élémentaires totales - Partie 1 : Mise en solution par l'acide fluorhydrique et l'acide perchlorique, (2001) 11.

[41] G. Grosse, PC-Mos II, Tech. Univ. München Munich. (1993) 0–85.

[42] M. Fan, P. Yuan, T. Chen, H. He, A. Yuan, K. Chen, et al., Synthesis, characterization and size control of zerovalent iron nanoparticles anchored on montmorillonite, Chinese Sci. Bull. 55 (2010) 1092–1099. doi:10.1007/s11434-010-0062-1.

[43] J. Shen, Z. Li, Q. Yan, Y. Chen, Reactions of Bivalent Metal Ions with Borohydride in Aqueous Solution for the Preparation of Ultrafine Amorphous Alloy Particles, J. Phys.

Chem. 97 (1993) 8504–8511. doi:10.1021/j100134a020.

[44] J.T. Nurmi, P.G. Tratnyek, J.E. Amonette, K. Pecher, C. Wang, J.C. Linehan, et al., Characterization and Properties of Metallic Iron Nanoparticles : Spectroscopy , Electrochemistry , and Kinetics, Env. Sci Technol. 39 (2005) 1221–1230. doi:10.1021/es049190u.

[45] N. Duxin, O. Stephan, C. Petit, P. Bonville, C. Colliex, M.P. Pileni, Pure α-Fe Coated by an Fe1-xBx Alloy, Chem. Mater. 4756 (1997) 2096–2100. doi:10.1021/cm9701567.

[46] S. Linderoth, S. Mørup, Amorphous TM1xBx alloy particles prepared by chemical reduction (invited), J. Appl. Phys., Vol. 69 (1991) 5256–5261. doi:10.1063/1.348070.

[47] T. Kemény, I. Vincze, B. Fogarassy, S. Arajs, Structure and crystallization of Fe-B metallic glasses, Phys. Rev. B (Condensed Matter). 20 (1979) 476–488.

[48] S. Balakrishnan, M.J. Bonder, G.C. Hadjipanayis, Particle size effect on phase and magnetic properties of polymer-coated magnetic nanoparticles, J. Magn. Magn. Mater. 321 (2009) 117–122. doi:10.1016/j.jmmm.2008.08.055.

[49] F. Bødkert, S. Mørup, C.A. Oxborrow, S. Linderoth, M.B. Madsen, J.W. Niemansverdriet, Mossbauer studies of ultrafine iron-containing particles on a carbon support carbon support, J. Phys. Condens. Matter 4. 4 (1992) 6555–6568.

[50] L. Zhang, A. Manthiram, Ambient Temperature Synthesis of Fine Metal Particles in Montmorillonite Clay and Their Magnetic Properties, Nanostructured Mater. 7 (1996) 437–451. doi:10.1016/0965-9773(96)00015-3.

[51] W. Yan, A.A. Herzing, C.J. Kiely, W. -x. Zhang, Nanoscale zero-valent iron (nZVI): Aspects of the core-shell structure and reactions with inorganic species in water, J. Contam. Hydrol. 118 (2010) 96.

[52] J. Miltz, M. Perry, Evaluation of the performance of iron-based oxygen scavengers, with comments on their optimal applications, Packag. Technol. Sci. 18 (2005) 21–27.

doi:10.1002/pts.671.

[53] Y. Byun, D. Darby, K. Cooksey, P. Dawson, S. Whiteside, Development of oxygen scavenging system containing a natural free radical scavenger and a transition metal, Food Chem. 124 (2011) 615–619. doi:10.1016/j.foodchem.2010.06.084.

[54] F. Charles, J. Sanchez, N. Gontard, Absorption kinetics of oxygen and carbon dioxide scavengers as part of active modified atmosphere packaging, J. Food Eng. 72 (2006) 1–7. doi:10.1016/j.jfoodeng.2004.11.006.

[55] K.K. Gaikwad, S. Singh, Y.S. Lee, A pyrogallol-coated modified LDPE film as an oxygen scavenging film for active packaging materials, Prog. Org. Coatings. 111 (2017) 186–195. doi:10.1016/j.porgcoat.2017.05.016.

Figures caption

Figure 1: Typical XRD patterns obtained for (a) MMT an (b) Dried MMT-Fe particles.

Figure 2: Typical Mössbauer spectra of (a) Wet MMT-Fe and (b) nano-Fe samples at 5°K.

Figure 3: Overview of iron MMT-Fe and nano-Fe particles: HR-TEM (a), low-magnification TEM images of MMT-Fe particles (b & d) and Nano-Fe particles (e) and particle size distribution in MMT-Fe sample (c)

Figure 4: STEM-EDS elemental analysis mapping of MMT-Fe (A) and nano-Fe (B). (a) STEM. (b) Fe map. (c) Si map. (d) O map. (e) Fe + O map. (f) Si + O map. The average EDS spectra are shown at the bottom.

Figure 5: Examples of experimental headspace-O_2 depletion curves (right y-axis) and corresponding O_2 absorption curves (left y-axis) for A) Wet MMT-Fe and B) Dried MMT-Fe

Figure 6: Comparison of oxygen absorption curves for Wet MMT-Fe, Dried MMT-Fe and Stored MMT-Fe (A) full curve and (B) zoom on the first 5 hours

Figure 7: Initial slopes of the absorption curves for "wet", "dried", "stored" and "dispersed" MMT-Fe.

Figure 8: Mössbauer spectra at 5 K of wet (a), dried (b) MMT-Fe material before any air exposure. Spectra (c) to (h) were collected after air exposure for the indicated time.

Figure 9: Figure 3: Evaluation of iron species after air exposure. The initial wet composition is shown for comparison. (Note the logarithmic x-axis).

Figure 4: Prediction of O_2 absorption and residual active scavenger for "Dried" MMT-Fe, by using 2-species model (Eq. **5). (a) Comparison of experimental (grey dots) and predicted (black line) data for headspace-O_2 depletion curves. (b) Prediction of Fe (line) and $Fe(OH)_2$ (dashed line) content.**

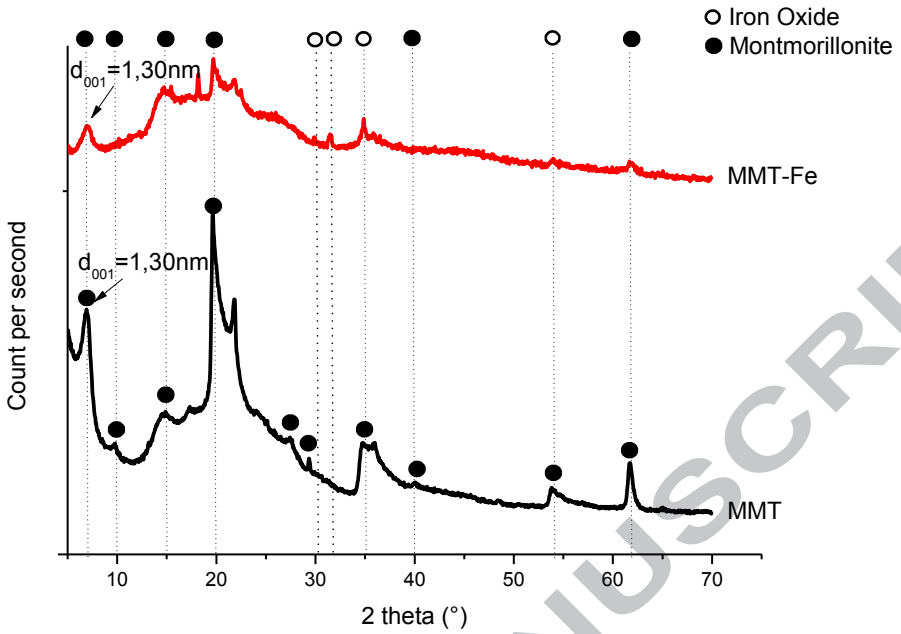

Figure 1: Typical XRD patterns obtained for (a) MMT an (b) Dried MMT-Fe particles.

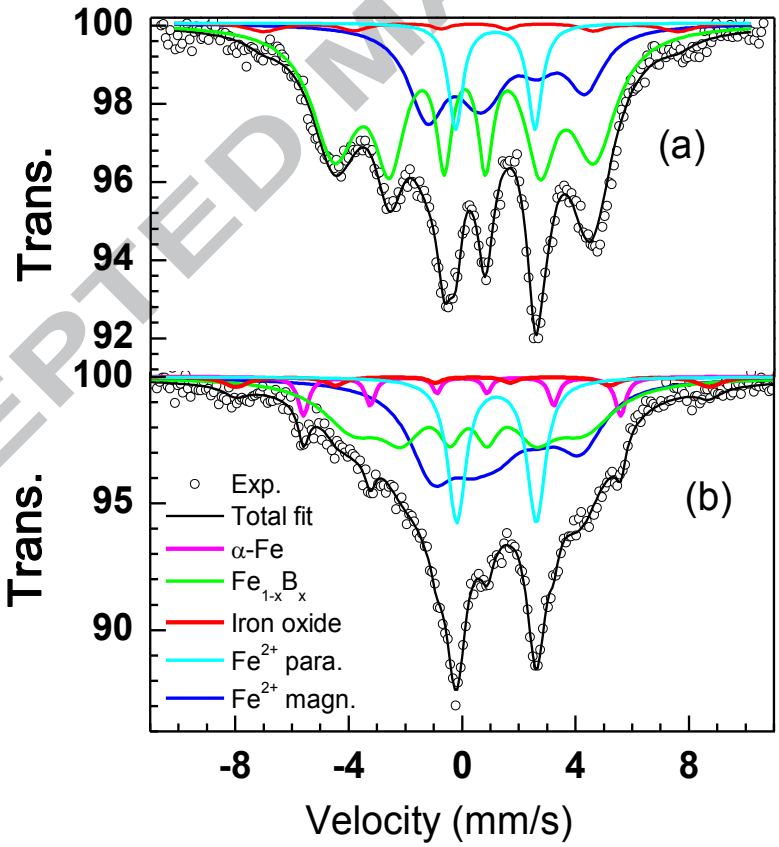

Figure 2: Typical Mössbauer spectra of (a) Wet MMT-Fe and (b) nano-Fe samples at 5°K.

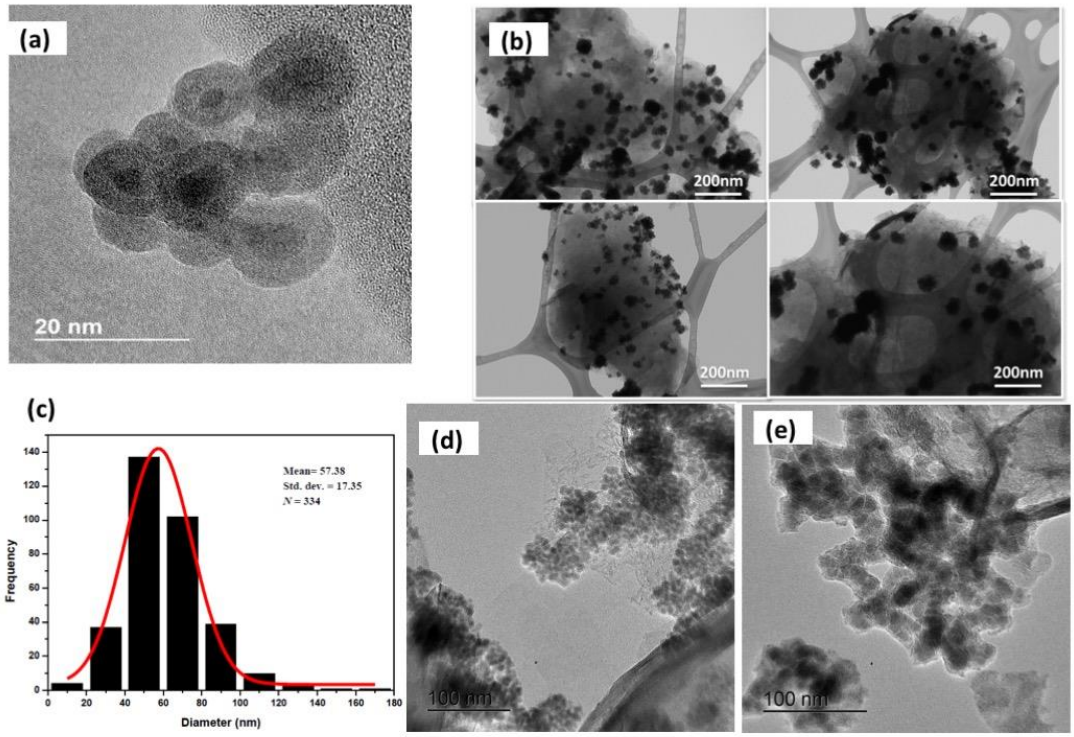

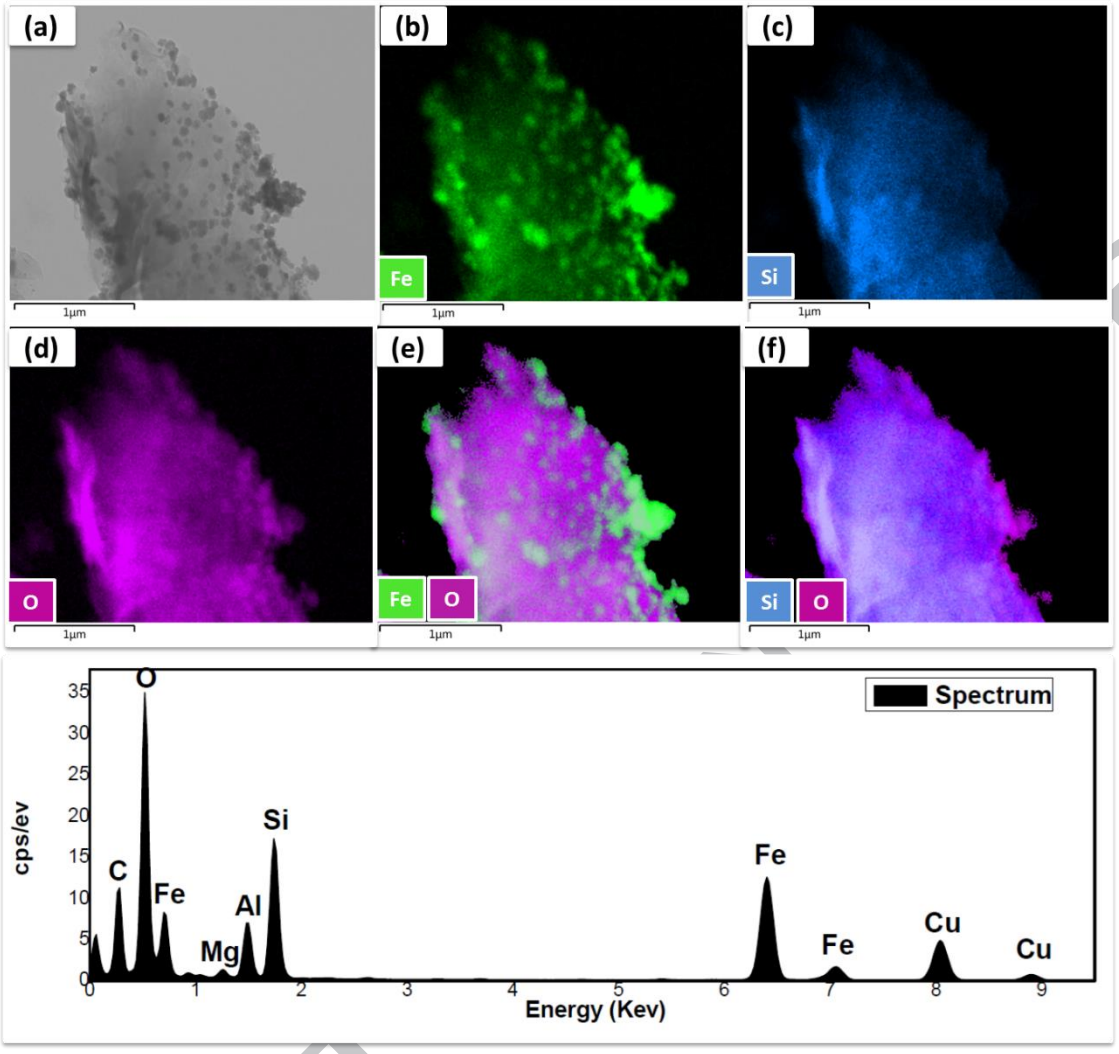

-A-

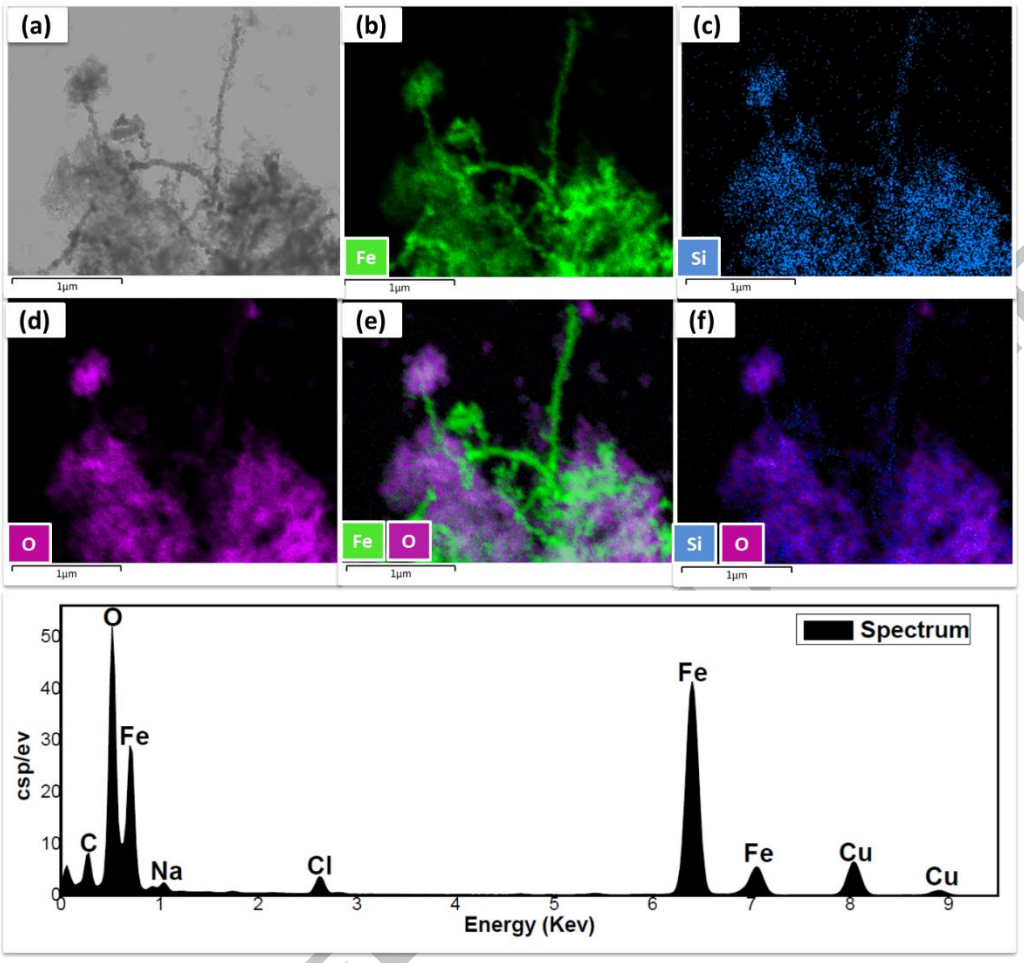

- B-

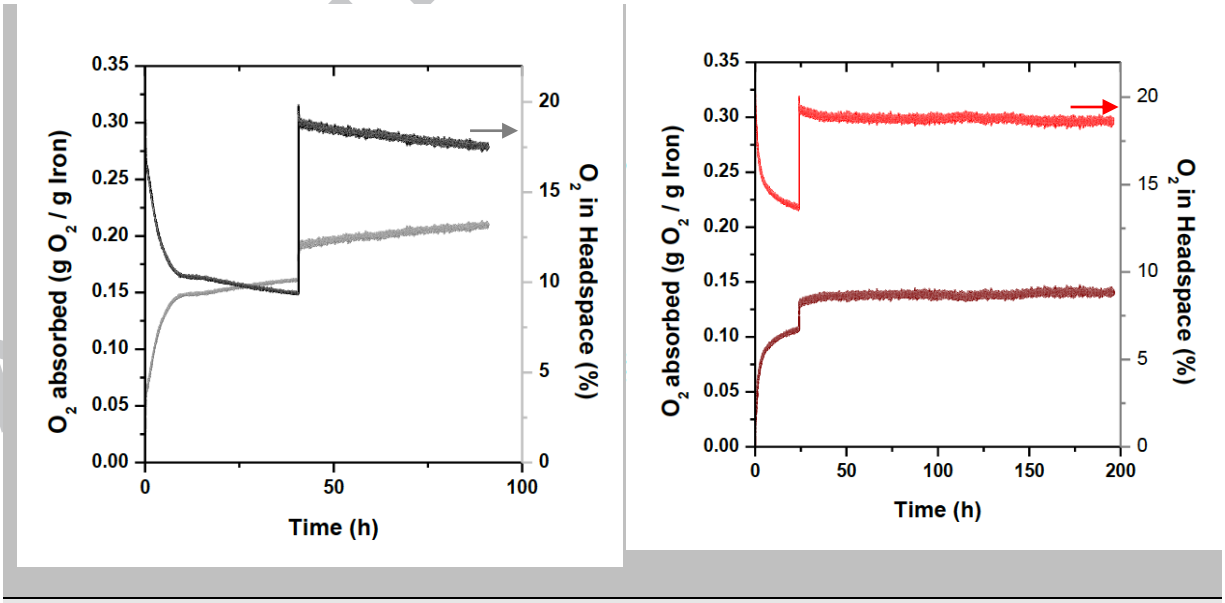

- A- - B-

Figure 5: Examples of experimental O_2 headspace depletion curves (right y-axis) and corresponding O_2 absorption curves (left y-axis) for A) Wet MMT-Fe and B) Dried MMT-Fe

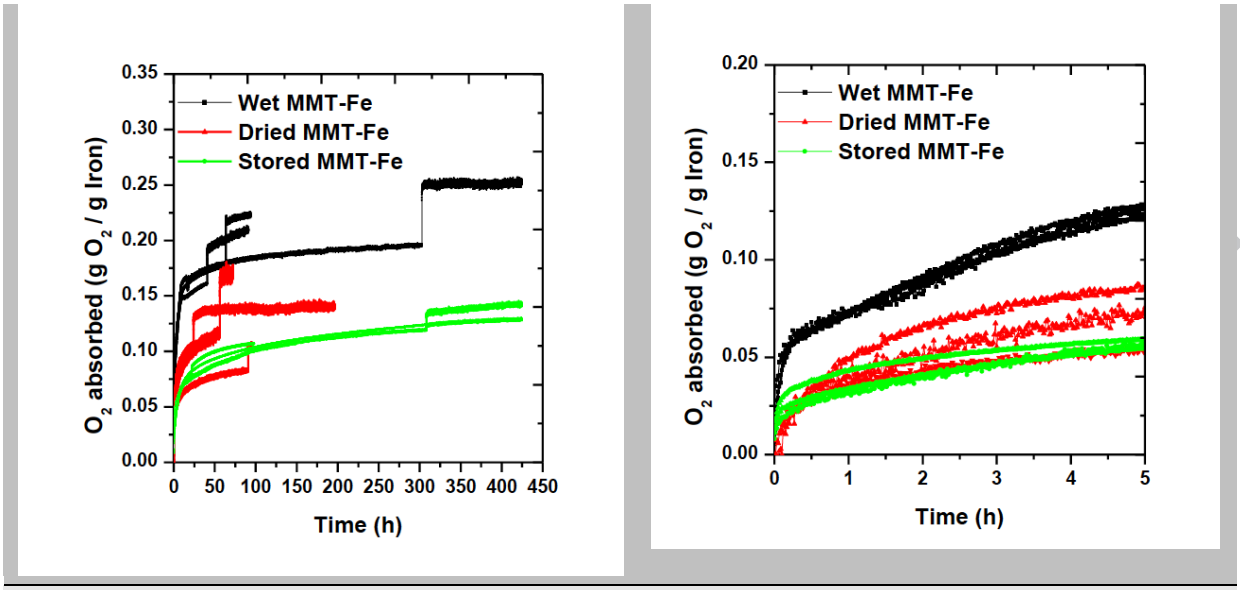

- A- - B-

Figure 6: Comparison of oxygen absorption curves for Wet MMT-Fe, Dried MMT-Fe and Stored MMT-Fe (A) full curve and (B) zoom on the first 5 hours

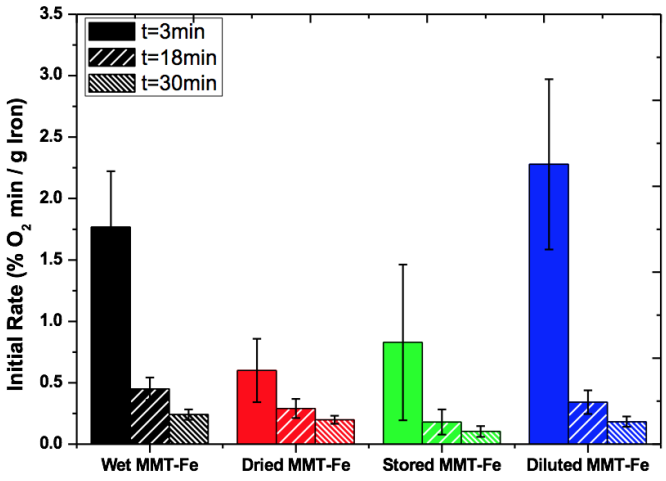

Figure 7: Initial slopes of the absorption curves for "wet", "dried", "stored" and "dispersed" MMT-Fe.

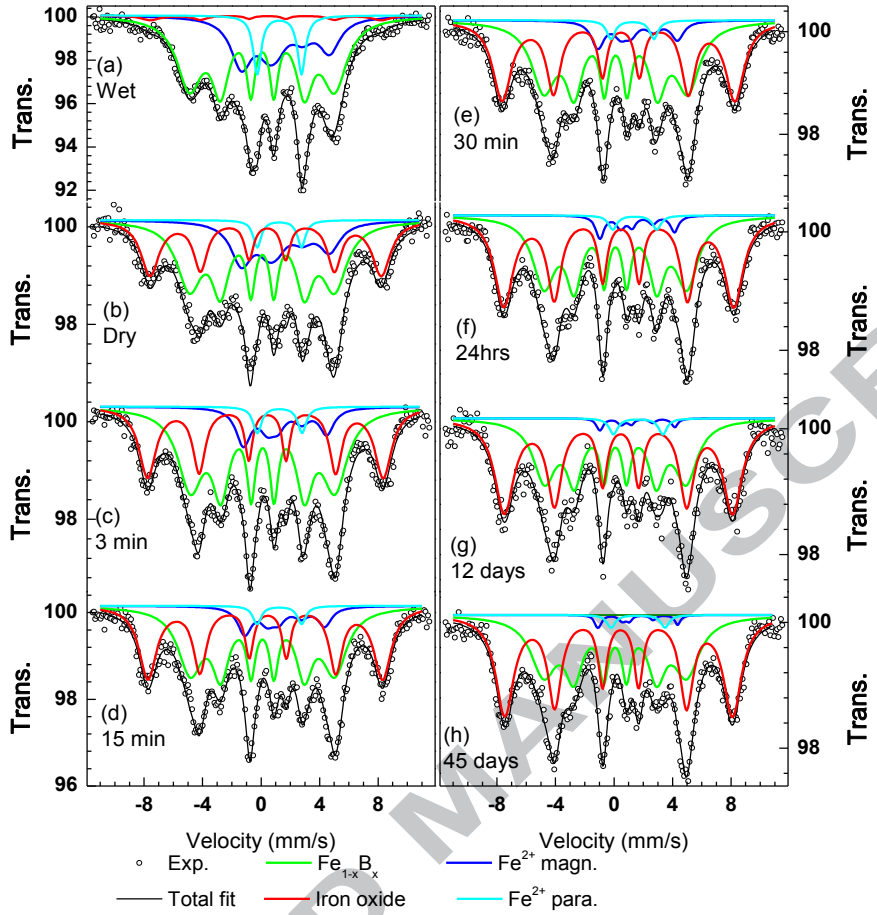

Figure 8: Mössbauer spectra at 5 K of wet (a), dried (b) MMT-Fe material before any air exposure. Spectra (c) to (h) were collected after air exposure for the indicated time.

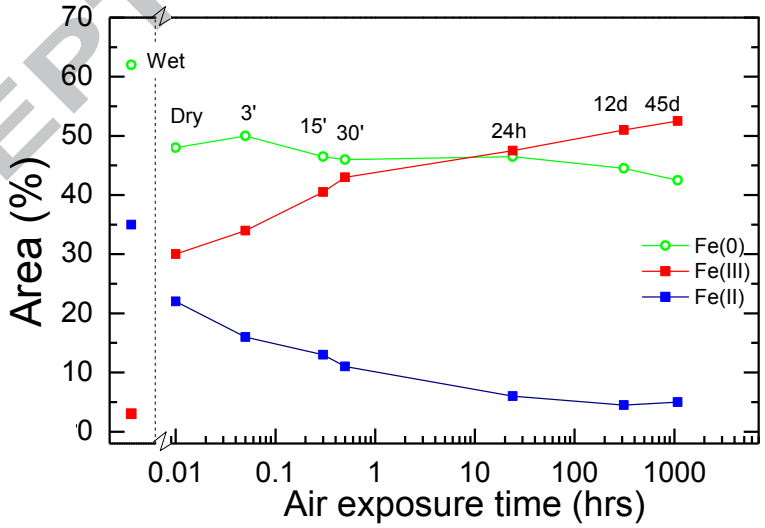

Figure 9: Evolution of iron species after air exposure. The initial wet composition is shown for comparison. (Note the logarithmic x-axis).

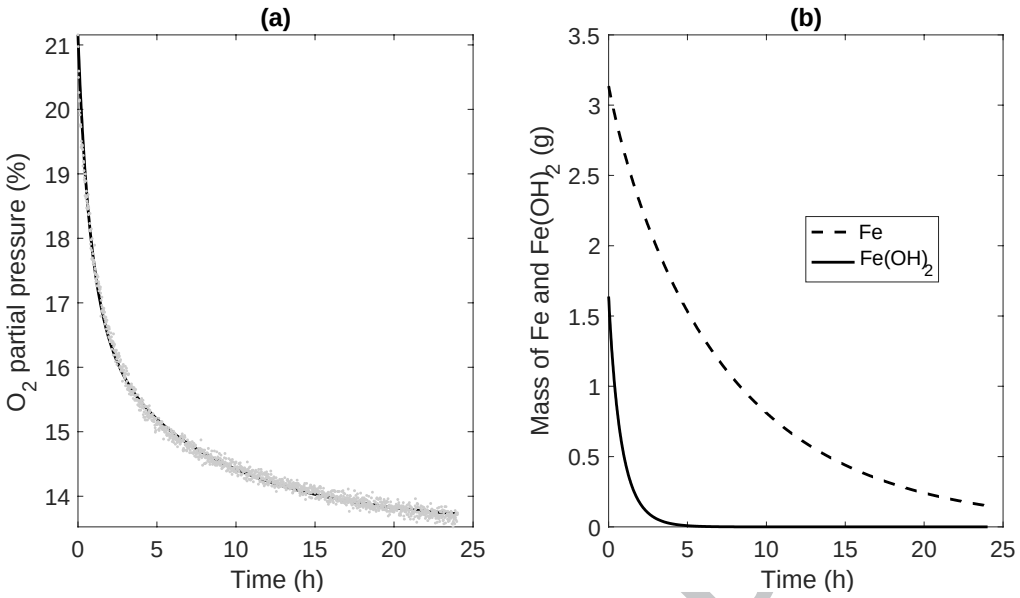

Figure 10: Prediction of O_2 absorption and residual active scavenger for "Dried" MMT-Fe, by using 2-species model (Eq. **5**)**. (a) Comparison of experimental (grey dots) and predicted (black line) data for O2 depletion curves. (b) Prediction of Fe (line) and $Fe(OH)_2$ (dashed line) content.**

Table 1. ^{57}Fe Mössbauer parameters at 5 K for "Wet" MMT-Fe and Nano-Fe

Sample	Comp.	IS (mm/s)	QS (mm/s)	LW (mm/s)	H (Tesla)	Area (%)
MMT-Fe	Fe^{2+} magn	1.21	-2.78	1.72	15.0	27
	$Fe_{1-x}B_x$	0.08	-0.03	0.47	30.8	62
	Fe^{3+} oxide	0.37	-0.12	0.60	49.0	3
	Fe^{2+} para	1.25	3.03	0.66	-	8
Nano-Fe	$Fe_{1-x}B_x$	0.34(4)	0.00	2.7(2)	25.2(2)	37(3)
	α-Fe	0.11(2)	0.00	0.46(7)	34.7(2)	5(1)
	Fe^{2+} para	1.32(1)	2.80(2)	0.77(4)	-	17(1)
	Fe^{2+} magn	1.31(5)	-2.8(2)	2.0(2)	11.7(6)	38(3)
	Fe^{3+} oxide	0.48(5)	0.00	1.0(5)	51.8(7)	3(1)

Table 2: Estimated parameters for 2-species model on wet and dried MMT-Fe. Mean ± standard deviation were calculated on 6 replicates.

	k_1 $(s^{-1}.mol^{-1})$	n_1 $(mol.mol^{-1})$	k_2 $(s^{-1}.mol^{-1})$	n_2 $(mol.mol^{-1})$	RMSE (% of O_2)

wet MMT-Fe	$2.9\ 10^{-6} \pm 3.5\ 10^{-6}$	0.47 ± 0.49	$1.8\ 10^{-4} \pm 2.4\ 10^{-4}$	0.39 ± 0.20	0.21 ± 0.09
dried MMT-Fe	$2.4\ 10^{-6} \pm 1.7\ 10^{-6}$	0.19 ± 0.07	$3.2\ 10^{-5} \pm 1.25\ 10^{-5}$	0.40 ± 0.13	0.11 ± 0.03

Highlights

- Iron nanoparticles on montmorillonite were synthetized using a chemical route
- ^{57}Fe Mössbauer spectroscopy evidences the formation of iron boride
- O_2 absorption kinetic was found to follow a second-order law
- ^{57}Fe Mössbauer permits to monitor apparition of iron oxides